

Neutron matter from chiral effective field theory interactions

T. Krüger,^{1,2,*} I. Tews,^{1,2,†} K. Hebeler,^{3,‡} and A. Schwenk^{2,1,§}

¹*Institut für Kernphysik, Technische Universität Darmstadt, 64289 Darmstadt, Germany*

²*ExtreMe Matter Institute EMMI, GSI Helmholtzzentrum für Schwerionenforschung GmbH, 64291 Darmstadt, Germany*

³*Department of Physics, The Ohio State University, Columbus, OH 43210, USA*

The neutron-matter equation of state constrains the properties of many physical systems over a wide density range and can be studied systematically using chiral effective field theory (EFT). In chiral EFT, all many-body forces among neutrons are predicted to next-to-next-to-next-to-leading order (N³LO). We present details and additional results of the first complete N³LO calculation of the neutron-matter energy, which includes the subleading three-nucleon as well as the leading four-nucleon forces, and provides theoretical uncertainties. In addition, we discuss the impact of our results for astrophysics: for the supernova equation of state, the symmetry energy and its density derivative, and for the structure of neutron stars. Finally, we give a first estimate for the size of the N³LO many-body contributions to the energy of symmetric nuclear matter, which shows that their inclusion will be important in nuclear structure calculations.

PACS numbers: 21.65.Cd, 12.39.Fe, 21.30.-x, 26.60.Kp

I. INTRODUCTION

Chiral effective field theory (EFT) provides a systematic expansion for nuclear forces including theoretical uncertainties [1], where the development and applications of three-nucleon (3N) forces are a frontier [2]. In this context, neutron matter constitutes a unique laboratory for chiral EFT, because all many-body forces are predicted to N³LO [3]. This offers the possibility to provide reliable constraints based on chiral EFT interactions for neutron-rich matter in astrophysics, for the equation of state, the symmetry energy and its density dependence, and for the structure of neutron stars [4, 5], but also allows us to test the chiral EFT power counting and the hierarchy of many-body forces over a wide density range. In addition, the prediction of many-body forces makes neutron-rich nuclei very exciting to test chiral EFT interactions against experiments at rare isotope beam facilities [6–21].

Neutron matter has been studied in chiral EFT using lattice simulations [22] and based on in-medium chiral perturbation theory [23, 24]. In addition, neutron matter has been calculated using renormalization-group-evolved chiral EFT interactions [4], where the renormalization group (RG) evolution improves the convergence of the many-body expansion around the Hartree-Fock energy [25, 26] and in a chiral Fermi liquid approach [27]. These studies demonstrated that 3N forces are significant at nuclear densities and that the dominant uncertainty is due to the truncation of 3N forces at the next-to-next-to-leading-order (N²LO) level [4]. Moreover, first Quantum Monte Carlo calculations with chiral EFT interactions

are providing nonperturbative benchmarks for neutron matter at nuclear densities [28].

Motivated by these studies and by the derivation of the parameter-free N³LO 3N and four-nucleon (4N) interactions [29–33], we recently presented the first calculation of the neutron-matter energy that includes all two-nucleon (NN), 3N and 4N forces consistently to N³LO [3]. In this paper, we discuss details of our complete N³LO calculation and present additional results as well as applications to astrophysics, for the equation of state and for the mass-radius relation of neutron stars. In addition, we give a first estimate for the size of the N³LO many-body contributions to the energy of symmetric nuclear matter in the Hartree-Fock approximation. This presents only a first step towards a complete calculation of nuclear matter, where contributions from many-body forces beyond Hartree-Fock are considerably more important than for neutron matter [34]. Our first results show that the inclusion of N³LO 3N forces will be important in nuclear structure calculations.

This paper is organized as follows. In Sec. II we discuss the chiral EFT interactions included in this work. Details of the many-body calculation and convergence are given in Sec. III. Our results for neutron matter are presented in Sec. IV, including a detailed discussion of the uncertainties. In Sec. V, we apply our results to the equation of state, in particular to the symmetry energy and its density dependence, and discuss the resulting constraints for the structure of neutron stars. We show first results for the N³LO 3N and 4N contributions in symmetric nuclear matter at the Hartree-Fock level in Sec. VI. Finally, we summarize and give an outlook.

* E-mail: tkrueger@theorie.ikp.physik.tu-darmstadt.de

† E-mail: tews@theorie.ikp.physik.tu-darmstadt.de

‡ E-mail: hebeler.4@osu.edu

§ E-mail: schwenk@physik.tu-darmstadt.de

TABLE I. Spin-independent and spin-dependent two-body contact couplings C_S and C_T , respectively, for the N^3 LO NN potentials of Refs. [36–38].

NN potential	C_S [fm ²]	C_T [fm ²]
EGM 450/500 MeV [36]	−4.19	−0.45
EGM 450/700 MeV [36]	−4.71	−0.24
EM 500 MeV [37, 38]	−3.90	0.22
EGM 550/600 MeV [36]	−1.24	0.36
EGM 600/600 MeV [36]	3.45	2.07
EGM 600/700 MeV [36]	1.31	1.00
EM 600 MeV [37, 38]	−3.88	0.28

II. CHIRAL EFT INTERACTIONS

A. N^2 LO and N^3 LO NN forces

The largest interaction contributions to the neutron-matter energy arise from NN forces. For our past applications of chiral EFT interactions to nucleonic matter [4, 34], the RG evolution has been used to evolve NN potentials to low-momentum interactions to improve the many-body convergence [25, 26]. In this work, we present calculations based directly on chiral EFT interactions without RG evolution and study the perturbative convergence following Ref. [3].

We investigate all existing NN potentials at N^2 LO and at N^3 LO of Epelbaum, Glöckle, and Meißner (EGM) [35, 36] with cutoffs $\Lambda/\tilde{\Lambda} = 450/500, 450/700, 550/600, 600/600$ and $600/700$ MeV, where Λ and $\tilde{\Lambda}$ denote the cutoff in the Lippmann-Schwinger equation and in the two-pion-exchange spectral-function regularization, respectively; as well as the available N^3 LO NN potentials of Entem and Machleidt (EM) [37, 38] with cutoffs $\Lambda = 500$ and 600 MeV. The EM 500 MeV potential is most commonly used in nuclear structure calculations, while the EGM potentials have only been studied in some many-body calculations [34], although they allow to explore a wider cutoff range.

The N^3 LO 3N and 4N forces involve the momentum-independent NN contact interactions $C_S + C_T \boldsymbol{\sigma}_1 \cdot \boldsymbol{\sigma}_2$. In particular, they mainly depend on C_T . The C_S and C_T values of the different N^3 LO NN potentials are listed in Table I for the neutron-proton case (the charge dependence contributes to higher-order charge-dependent 3N forces). For a perturbative calculation, we require Wigner symmetry ($C_T = 0$) to be fulfilled approximately at the interaction level. This is not the case for the EGM potentials with cutoffs 600/600 and 600/700 MeV, which have large spin-dependent couplings $C_T \sim C_S$ (and even a repulsive spin-independent C_S), and would lead to large C_T -dependent 3N forces at N^3 LO.

TABLE II. Values of couplings c_1 and c_3 for the different NN potentials, as well as from Krebs, Gasparyan, and Epelbaum (KGE, Ref. [43]), and the range adopted in this work.

	c_1 [GeV ^{−1}]	c_3 [GeV ^{−1}]
N^2 LO/ N^3 LO EGM NN [35, 36]	−0.81	−3.40
N^3 LO EM NN [37, 38]	−0.81	−3.20
N^2 LO KGE [43]	−(0.26–0.58)	−(2.80–3.14)
‘ N^2 LO’ KGE (recom.) [43]	−(0.37–0.73)	−(2.71–3.38)
N^3 LO KGE [43]	−(0.75–1.13)	−(4.77–5.51)
N^2 LO this work	−(0.37–0.81)	−(2.71–3.40)
N^3 LO this work	−(0.75–1.13)	−(4.77–5.51)

B. N^2 LO 3N forces

Three-nucleon forces enter at N^2 LO in the chiral EFT expansion without explicit Deltas [39, 40]. Due to the Pauli principle and the coupling of pions to spin, only the c_1 and c_3 parts of the long-range two-pion-exchange 3N interactions contribute at N^2 LO [4] (see also Ref. [41]). The same c_i couplings also enter NN interactions at N^2 LO and have been determined from pion-nucleon or NN scattering. The c_1 and c_3 values used in chiral NN potentials are given in Table II. Note, however, that the range adopted in the NN potentials of Table II does not reflect the allowed range for the c_i couplings, which are not satisfactorily constrained at present, e.g., with a range of $c_3 = -(3.2–5.9)$ GeV^{−1} from different theoretical analyses (see Table I in Ref. [2]).

We see from Table II that, while the c_1 value is of natural size, the c_3 value is large. This is due to the single- Δ excitation, which enhances $c_3 \sim 1/(m_\Delta - m)$ by the Δ -nucleon mass difference to a large value ($c_1 = 0$ for a single- Δ excitation). In chiral EFT with explicit Δ ’s, the single- Δ contribution would in fact be included at one order lower; at next-to-leading order (NLO) in this case. The large c_3 value has two effects. First, it leads to a slower convergence at the order when the c_i contributions enter. This corresponds to topologies where Δ excitations are important. This can already be seen in the convergence pattern with NN interactions, where the leading two-pion-exchange NN interaction at NLO receives large contributions due to the large c_i that enter the subleading two-pion-exchange NN interaction at N^2 LO [1, 42]. Therefore, for 3N and 4N forces important contributions to the N^3 LO interactions studied here can be expected in topologies where the c_i couplings enter at N^4 LO [43, 44]. This convergence pattern can be improved by including the Δ explicitly in chiral EFT. Second, the large c_3 coupling in the N^2 LO 3N interaction also worsens the perturbative convergence of the many-body expansion around the Hartree-Fock energy. This is most important for the large c_3 values considered in the N^3 LO calculation of this work (see Table II).

In addition, we list in Table II the c_i values extracted from a high-order analysis up to N^4 LO of Krebs, Gas-

parayan, and Epelbaum (KGE, Ref. [43]). The KGE ranges at N²LO and N³LO are given in Table II, in addition to values recommended to be used in an N²LO calculation that are tuned to capture the higher-order result. In this work, we take the KGE recommended c_i range for the N²LO calculation, minimally enlarged to include the c_i values of the NN potentials, and the KGE N³LO c_i range for our complete N³LO calculation. Note the large c_3 value for the latter, which is still in the range of Table I in Ref. [2]. We thus explore c_i values in the many-body interactions without varying the c_i in the NN potential. This is because changing the c_i in the NN potential would also require an adjustment of other couplings in the fit to NN data. We expect that some of the changes can be absorbed by the N³LO NN contact interactions, but it is very important to develop new N³LO NN potentials that can explore this sensitivity.

C. N³LO 3N and 4N forces

The many-body forces at N³LO are predicted by couplings in previous orders of the chiral EFT expansion. Hence, there are no new parameters for N³LO 3N and 4N interactions [1]. The subleading N³LO 3N forces have been derived recently [29–31]. They can be grouped into five topologies, where the latter two depend on the NN contact couplings C_T and C_S (see the Appendix):

$$V_{3N}^{\text{N}^3\text{LO}} = V^{2\pi} + V^{2\pi-1\pi} + V^{\text{ring}} + V^{2\pi-\text{cont}} + V^{1/m}. \quad (1)$$

Here, $V^{2\pi}$, $V^{2\pi-1\pi}$, and V^{ring} denote the long-range two-pion-exchange, the two-pion-one-pion-exchange, and the pion-ring 3N interactions, respectively [30]. The terms $V^{2\pi-\text{cont}}$ and $V^{1/m}$ are the short-range two-pion-exchange-contact 3N interaction and 3N relativistic corrections, respectively [31]. The latter are small [3] and depend also on the constants β_8 and β_9 , which need to be chosen consistently with the unitary transformation used for the NN potentials [31]. In addition, there could be short-range one-pion-exchange-contact 3N interactions, but they have been shown to vanish at N³LO [31].

According to the chiral power counting, 4N forces enter at N³LO. They have been derived in Refs. [32, 33] and depend also on the contact coupling C_T , but in neutron matter the C_T -dependent parts do not contribute. There are seven 4N topologies that lead to non-vanishing contributions. In neutron matter only two three-pion-exchange diagrams (in Ref. [32] named V^a and V^e) and the pion-pion-interaction diagram (V^f) contribute [3].

III. MANY-BODY DETAILS

A. Hartree Fock

We calculate the energy per particle at the Hartree-Fock level and include contributions beyond Hartree Fock

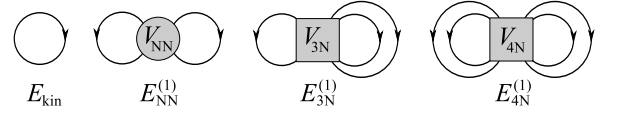


FIG. 1. Diagrams contributing to the Hartree-Fock energy. These include the kinetic energy E_{kin} and the first-order NN, 3N, and 4N interaction energies $E_{\text{NN}}^{(1)}$, $E_{3\text{N}}^{(1)}$, and $E_{4\text{N}}^{(1)}$.

using many-body perturbation theory [4, 25, 34]. The Hamiltonian is given by $H = T + V_{\text{NN}} + V_{3\text{N}} + V_{4\text{N}}$, where T is the kinetic energy and V_{NN} , $V_{3\text{N}}$, and $V_{4\text{N}}$ denote the NN, 3N, and 4N interactions, respectively. The Hartree-Fock contributions are shown diagrammatically in Fig. 1. At this level, the contribution of the A -nucleon interaction to the energy per particle is given by

$$\begin{aligned} \frac{E_{\text{AN}}^{(1)}}{N} &= \frac{1}{n} \frac{1}{A!} \sum_{\sigma_1, \dots, \sigma_A} \int \frac{d\mathbf{k}_1}{(2\pi)^3} \cdots \int \frac{d\mathbf{k}_A}{(2\pi)^3} f_R^2 n_{\mathbf{k}_1} \cdots n_{\mathbf{k}_A} \\ &\times \langle 1 \dots A | \mathcal{A}_A \sum_{i_1 \neq \dots \neq i_A}^A V_{\text{AN}}(i_1, \dots, i_A) | 1 \dots A \rangle, \quad (2) \end{aligned}$$

with density n and short-hand notation $i \equiv \mathbf{k}_i \sigma_i$. Here, \mathcal{A}_A denotes the A -body antisymmetrizer and $n_{\mathbf{k}_i} = \theta(k_F - k_i)$ the Fermi-Dirac distribution at zero temperature. For the many-body forces, we use a Jacobi-momenta regulator. In terms of \mathbf{k}_i , this is given by

$$f_R = e^{-[(k_1^2 + \dots + k_A^2 - \mathbf{k}_1 \cdot \mathbf{k}_2 - \dots - \mathbf{k}_{A-1} \cdot \mathbf{k}_A)/(AA^2)]^{n_{\text{exp}}}}, \quad (3)$$

where we take $n_{\text{exp}} = 4$ and consider 3N/4N cutoffs $\Lambda = 2 - 2.5 \text{ fm}^{-1}$. This cutoff range allows to probe the sensitivity to short-range many-body forces within the limits of the employed power counting. For the evaluation of 3N/4N forces, we use for the nucleon and pion mass, $m = 938.92 \text{ MeV}$ and $m_\pi = 138.04 \text{ MeV}$, for the axial coupling $g_A = 1.29$, and for the pion decay constant $f_\pi = 92.4 \text{ MeV}$ [30–33, 40].

As an example, we present details of the derivation of the Hartree-Fock energy from the N³LO two-pion-exchange 3N interactions. Their contributions can be grouped into two parts: one that shifts the c_i couplings of the N²LO 3N forces and a part

$$\begin{aligned} V_{2\pi}^{(4)} &= \frac{g_A^4}{256\pi f_\pi^6} \sum_{i \neq j \neq k} \frac{(\boldsymbol{\sigma}_i \cdot \mathbf{q}_i)(\boldsymbol{\sigma}_j \cdot \mathbf{q}_j)}{(\mathbf{q}_i^2 + m_\pi^2)(\mathbf{q}_j^2 + m_\pi^2)} \\ &\times \left[m_\pi(m_\pi^2 + 3q_i^2 + 3q_j^2 + 4\mathbf{q}_i \cdot \mathbf{q}_j) \right. \\ &+ (2m_\pi^2 + q_i^2 + q_j^2 + 2\mathbf{q}_i \cdot \mathbf{q}_j) \\ &\times (3m_\pi^2 + 3q_i^2 + 3q_j^2 + 4\mathbf{q}_i \cdot \mathbf{q}_j) A(q_k) \left. \right], \\ &= \sum_{i \neq j \neq k} (\boldsymbol{\sigma}_i \cdot \mathbf{q}_i)(\boldsymbol{\sigma}_j \cdot \mathbf{q}_j) F_{2\pi}^{(4)}(\mathbf{q}_i, \mathbf{q}_j). \quad (4) \end{aligned}$$

For the isospin part we have used that for neutrons

$$\langle nnn | \boldsymbol{\tau}_i \cdot \boldsymbol{\tau}_j | nnn \rangle = 1, \quad (5)$$

$$\langle nnn | \boldsymbol{\tau}_i \cdot \boldsymbol{\tau}_j \times \boldsymbol{\tau}_k | nnn \rangle = 0, \quad (6)$$

and introduced the function $F_{2\pi}^{(4)}(\mathbf{q}_i, \mathbf{q}_j)$, which absorbs all parts of the interaction except for the spin dependencies. Furthermore, $\mathbf{q}_i = \mathbf{k}'_i - \mathbf{k}_i$ and for $F_{2\pi}^{(4)}$ we use $\mathbf{q}_1 + \mathbf{q}_3 = -\mathbf{q}_2$ due to momentum conservation. Since the particles i, j, k are all neutrons and we sum over all possible spin states, the six different terms in the sum lead to identical contributions and we can write

$$V_{2\pi}^{(4)} = 6(\boldsymbol{\sigma}_1 \cdot \mathbf{q}_1)(\boldsymbol{\sigma}_3 \cdot \mathbf{q}_3) F_{2\pi}^{(4)}(\mathbf{q}_1, \mathbf{q}_3). \quad (7)$$

For the spin trace $\text{Tr}_\sigma \langle 123 | \mathcal{A}_3 V_{2\pi}^{(4)} | 123 \rangle$ we use that Pauli matrices are traceless and the relation $\sigma_i^a \sigma_i^b = \delta^{ab} + i\epsilon^{abc} \sigma_i^c$. Thus, only the parts of the antisymmetrizer that contain the same-particle Pauli matrices as the potential need to be considered. In this case, the terms must contain $\boldsymbol{\sigma}_1$ and $\boldsymbol{\sigma}_3$ but not $\boldsymbol{\sigma}_2$. The antisymmetrizer is given by

$$\mathcal{A}_3 = 1 - P_{12} - P_{13} - P_{23} + P_{12}P_{23} + P_{13}P_{23}, \quad (8)$$

with $P_{ij} = P_{ij}^k \frac{1+\boldsymbol{\sigma}_i \cdot \boldsymbol{\sigma}_j}{2}$, where P_{ij}^k exchanges the momenta of particles i and j . The last two terms can be written as

$$\begin{aligned} P_{12}P_{23} &= \frac{1}{4} P_{12}^k P_{23}^k (1 + \boldsymbol{\sigma}_1 \cdot \boldsymbol{\sigma}_2 + \boldsymbol{\sigma}_2 \cdot \boldsymbol{\sigma}_3 \\ &\quad + \boldsymbol{\sigma}_1 \cdot \boldsymbol{\sigma}_3 + i\boldsymbol{\sigma}_1 \cdot \boldsymbol{\sigma}_3 \times \boldsymbol{\sigma}_2), \\ P_{13}P_{23} &= \frac{1}{4} P_{13}^k P_{13}^k (1 + \boldsymbol{\sigma}_1 \cdot \boldsymbol{\sigma}_2 + \boldsymbol{\sigma}_2 \cdot \boldsymbol{\sigma}_3 \\ &\quad + \boldsymbol{\sigma}_1 \cdot \boldsymbol{\sigma}_3 + i\boldsymbol{\sigma}_1 \cdot \boldsymbol{\sigma}_2 \times \boldsymbol{\sigma}_3). \end{aligned} \quad (9)$$

Thus, the only relevant terms of the antisymmetrizer are

$$\left(-\frac{P_{13}^k}{2} + \frac{P_{12}^k P_{23}^k}{4} + \frac{P_{13}^k P_{23}^k}{4} \right) \boldsymbol{\sigma}_1 \cdot \boldsymbol{\sigma}_3. \quad (10)$$

Multiplying this spin part with the potential leads to

$$\begin{aligned} \text{Tr}_\sigma [\boldsymbol{\sigma}_1 \cdot \boldsymbol{\sigma}_3 V_{2\pi}^{(4)}] &= \text{Tr}_\sigma \left[6 \sigma_1^a \sigma_3^a \sigma_1^b q_1^b \sigma_3^c q_3^c F_{2\pi}^{(4)}(\mathbf{q}_1, \mathbf{q}_3) \right], \\ &= \text{Tr}_\sigma \left[6(\delta^{ab} + i\epsilon^{abd} \sigma_1^d)(\delta^{ac} + i\epsilon^{ace} \sigma_3^e) \right. \\ &\quad \left. \times q_1^b q_3^c F_{2\pi}^{(4)}(\mathbf{q}_1, \mathbf{q}_3) \right]. \end{aligned} \quad (11)$$

All terms containing Pauli matrices vanish when taking the trace, so

$$\text{Tr}_\sigma [\boldsymbol{\sigma}_1 \cdot \boldsymbol{\sigma}_3 V_{2\pi}^{(4)}] = 8 \cdot 6 \mathbf{q}_1 \cdot \mathbf{q}_3 F_{2\pi}^{(4)}(\mathbf{q}_1, \mathbf{q}_3). \quad (12)$$

Thus, we obtain

$$\begin{aligned} \text{Tr}_\sigma \mathcal{A}_3 V_{2\pi}^{(4)} &= 8 \cdot 6 \left(-\frac{P_{13}^k}{2} + \frac{P_{12}^k P_{23}^k}{4} + \frac{P_{13}^k P_{23}^k}{4} \right) \\ &\quad \times \mathbf{q}_1 \cdot \mathbf{q}_3 F_{2\pi}^{(4)}(\mathbf{q}_1, \mathbf{q}_3). \end{aligned} \quad (13)$$

Putting everything together yields for the spin-summed antisymmetrized matrix element

$$\begin{aligned} \langle V_{2\pi}^{(4)} \rangle &= \frac{1}{3!} \text{Tr}_\sigma \langle 123 | \mathcal{A}_3 V_{2\pi}^{(4)} | 123 \rangle = 8 \langle 123 | \left(-\frac{P_{13}^k}{2} + \frac{P_{12}^k P_{23}^k}{4} + \frac{P_{13}^k P_{23}^k}{4} \right) \mathbf{q}_1 \cdot \mathbf{q}_3 F_{2\pi}^{(4)}(\mathbf{q}_1, \mathbf{q}_3) | 123 \rangle, \\ &= -4 \mathbf{k}_{31} \cdot \mathbf{k}_{13} F_{2\pi}^{(4)}(\mathbf{k}_{31}, \mathbf{k}_{13}) + 2 \mathbf{k}_{21} \cdot \mathbf{k}_{13} F_{2\pi}^{(4)}(\mathbf{k}_{21}, \mathbf{k}_{13}) + 2 \mathbf{k}_{31} \cdot \mathbf{k}_{23} F_{2\pi}^{(4)}(\mathbf{k}_{31}, \mathbf{k}_{23}), \\ &= 4 \left[k_{13}^2 F_{2\pi}^{(4)}(-\mathbf{k}_{13}, \mathbf{k}_{13}) - \mathbf{k}_{12} \cdot \mathbf{k}_{13} F_{2\pi}^{(4)}(-\mathbf{k}_{12}, \mathbf{k}_{13}) \right], \end{aligned} \quad (14)$$

where $\mathbf{k}_{ij} = \mathbf{k}_i - \mathbf{k}_j$, and we have relabeled the momentum indices in the last step, because the momentum integrals are equal for the three neutrons and the regulator is symmetric under exchange of the momenta.

Analogously, we obtain the expressions for the other $N^3\text{LO}$ 3N- and 4N-interaction matrix elements at the Hartree-Fock level. They are given in Appendix A. The analytic derivations have been checked independently and by using an automated Mathematica routine for the spin traces.

B. Beyond Hartree Fock

For nucleonic matter based on chiral EFT interactions, contributions beyond the Hartree-Fock level are important [4, 25, 34]. The dominant contribution to the energy is due to NN-NN correlations $[E_1^{(2)}]$. In addition, there are NN-3N correlations $[E_2^{(2)}$ and $E_3^{(2)}]$, 3N-3N correlations $[E_4^{(2)}$ and $E_5^{(2)}]$, where the $E_i^{(2)}$ follow the notation of Fig. 2, as well as NN-4N, 3N-4N and 4N-4N correla-

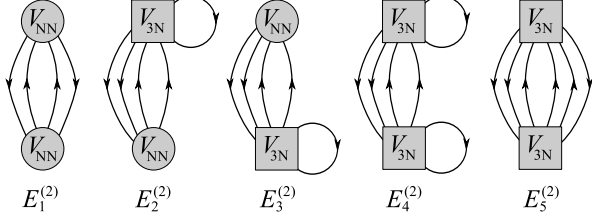


FIG. 2. Second-order contributions to the energy due to NN-NN correlations, $E_1^{(2)}$, NN-3N and 3N-3N correlations $E_{2/3}^{(2)}$ and $E_4^{(2)}$, where the 3N forces enter as density-dependent two-body interactions, as well as the residual 3N-3N contribution $E_5^{(2)}$ not considered here.

tions. Based on the results of Refs. [3, 4], we expect the residual 3N-3N contribution $E_5^{(2)}$ and all contributions including 4N interactions to be small.

The second-order contribution to the energy due to NN interactions and including 3N interactions as density-dependent two-body interactions is given by

$$\begin{aligned} \sum_{i=1}^4 E_i^{(2)} &= \frac{1}{4} \left[\prod_{i=1}^4 \sum_{\sigma_i} \int \frac{d^3 \mathbf{k}_i}{(2\pi)^3} \right] |\langle 12 | V_{\text{as}}^{(2)} | 34 \rangle|^2 \\ &\times \frac{n_{\mathbf{k}_1} n_{\mathbf{k}_2} (1 - n_{\mathbf{k}_3}) (1 - n_{\mathbf{k}_4})}{\varepsilon_{\mathbf{k}_1} + \varepsilon_{\mathbf{k}_2} - \varepsilon_{\mathbf{k}_3} - \varepsilon_{\mathbf{k}_4}} \\ &\times (2\pi)^3 \delta(\mathbf{k}_1 + \mathbf{k}_2 - \mathbf{k}_3 - \mathbf{k}_4), \end{aligned} \quad (15)$$

where $V_{\text{as}}^{(2)} = (1 - P_{12})V_{\text{NN}} + \bar{V}_{3\text{N}}$ is the antisymmetrized two-body interaction, which includes NN interactions and density-dependent two-body interactions from N²LO 3N forces [4]. The latter are obtained by summing the third particle over the occupied states in the Fermi sea

$$\bar{V}_{3\text{N}} = \sum_{\sigma_3} \int \frac{d^3 \mathbf{k}_3}{(2\pi)^3} n_{\mathbf{k}_3} \mathcal{A}_3 V_{3\text{N}}^{\text{N}^2\text{LO}} \Big|_{\text{nnn}}. \quad (16)$$

At third order, we include particle-particle diagrams as in Ref. [34]. Their size provides a test of the convergence of the many-body calculation. We divide the third-order particle-particle contributions into classes $E_i^{(3)}$, which are based on the $E_i^{(2)}$ of Fig. 2 by adding one additional ladder and vertex with anti-symmetrized effective two-body interactions $V_{\text{as}}^{(2)} = (1 - P_{12})V_{\text{NN}} + \bar{V}_{3\text{N}}$ to the different diagrams $E_i^{(2)}$.

C. Convergence

To study the perturbative convergence of the different NN potentials, we calculate the Hartree-Fock as well as second- and third-order energies with both free and Hartree-Fock single-particle energies. First, we consider NN interactions only and then study the changes when including also N²LO 3N forces. The results are shown

TABLE III. Maximal energy difference between the second- and third-order contributions using a Hartree-Fock spectrum for the second-order and a free or Hartree-Fock spectrum for the third-order calculation at saturation density. Results are given for the different N³LO NN potentials at the NN-only level and including the leading N²LO 3N forces with $\Lambda = 2.0 \text{ fm}^{-1}$, $c_1 = -0.75 \text{ GeV}^{-1}$ and $c_3 = -4.77 \text{ GeV}^{-1}$. The first three potentials exhibit a good convergence pattern with both NN-only and including N²LO 3N forces, and are therefore included in our complete N³LO calculation. Note that the N³LO EGM 600/600 and 600/700 potentials will not be considered in our complete N³LO calculation, because they have large C_T couplings (see the discussion of Table I).

N ³ LO NN potential	$ \Delta E_{\text{NN-only}}^{(2/3)} $	$ \Delta E_{\text{NN/3N}}^{(2/3)} $
EGM 450/500 MeV	0.8 MeV	0.6 MeV
EGM 450/700 MeV	0.4 MeV	0.4 MeV
EM 500 MeV	1.1 MeV	1.7 MeV
EGM 550/600 MeV	1.0 MeV	3.1 MeV
EGM 600/600 MeV	0.2 MeV	1.5 MeV
EGM 600/700 MeV	11.4 MeV	16.1 MeV
EM 600 MeV	7.7 MeV	9.1 MeV

in Figs. 3 and 4, respectively. The bands at each order range from using a free to a Hartree-Fock single-particle spectrum. In addition, we give in Table III the maximal difference between the Hartree-Fock-spectrum results at second order and those with a free or Hartree-Fock spectrum at third order for nuclear saturation density $n_0 = 0.17 \text{ fm}^{-3}$ (corresponding to a Fermi momentum $k_F = 1.7 \text{ fm}^{-1}$). We take this energy difference as a measure of convergence for the potentials, as it includes both the uncertainty due to different single-particle energies as well as the uncertainty in the convergence of the many-body calculation.

At the NN level in Fig. 3, the N³LO EGM potentials with cutoffs 450/500, 450/700, 550/600, and 600/600 MeV and the N³LO EM 500 MeV potential exhibit only small energy changes from second to third order. The larger-cutoff potentials (N³LO EGM 600/700 MeV and N³LO EM 600 MeV), however, show large changes from second to third order, as well as a large band for the range of single-particle energies (especially for the EM 600 MeV potential). This demonstrates that these potentials are nonperturbative, see also Table III.

The convergence pattern is similar when the leading N²LO 3N forces are included. We show the results at this N³LO NN and N²LO 3N level in Fig. 4 for a 3N cutoff $\Lambda = 2.0 \text{ fm}^{-1}$ and a particular choice of $c_1 = -0.75 \text{ GeV}^{-1}$ and $c_3 = -4.77 \text{ GeV}^{-1}$, although the general picture is unchanged for other coupling values.

We find almost no change in the convergence pattern of the N³LO EGM 450/500 and 450/700 MeV potentials; see Table III. This indicates that these potentials are perturbative for neutron matter. For the N³LO EGM 450/500 MeV potential, this is expected already from the small Weinberg eigenvalues in Ref. [26], which are a nec-

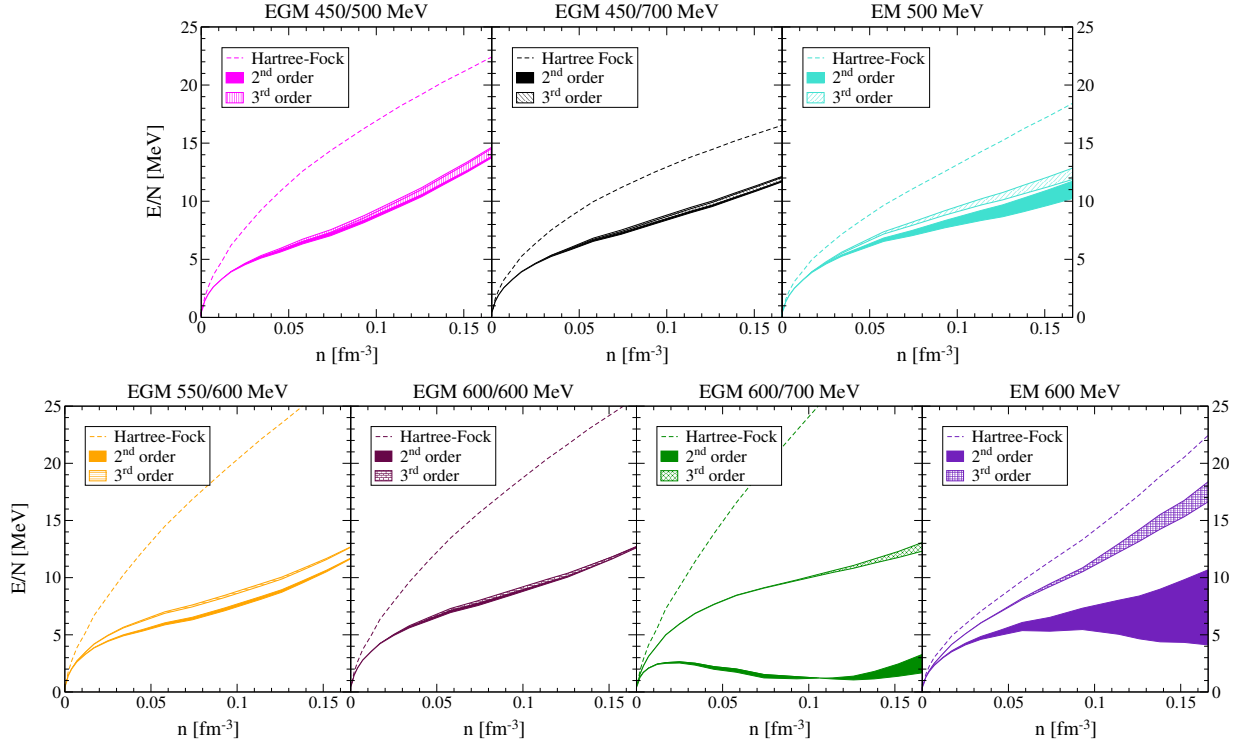


FIG. 3. (Color online) Energy per particle as a function of density for the different $N^3\text{LO}$ NN potentials of Refs. [35–38]. The dashed lines are Hartree-Fock results only. The filled and shaded bands are second- and third-order energies, respectively, where at each order the band ranges from using a free to a Hartree-Fock spectrum.

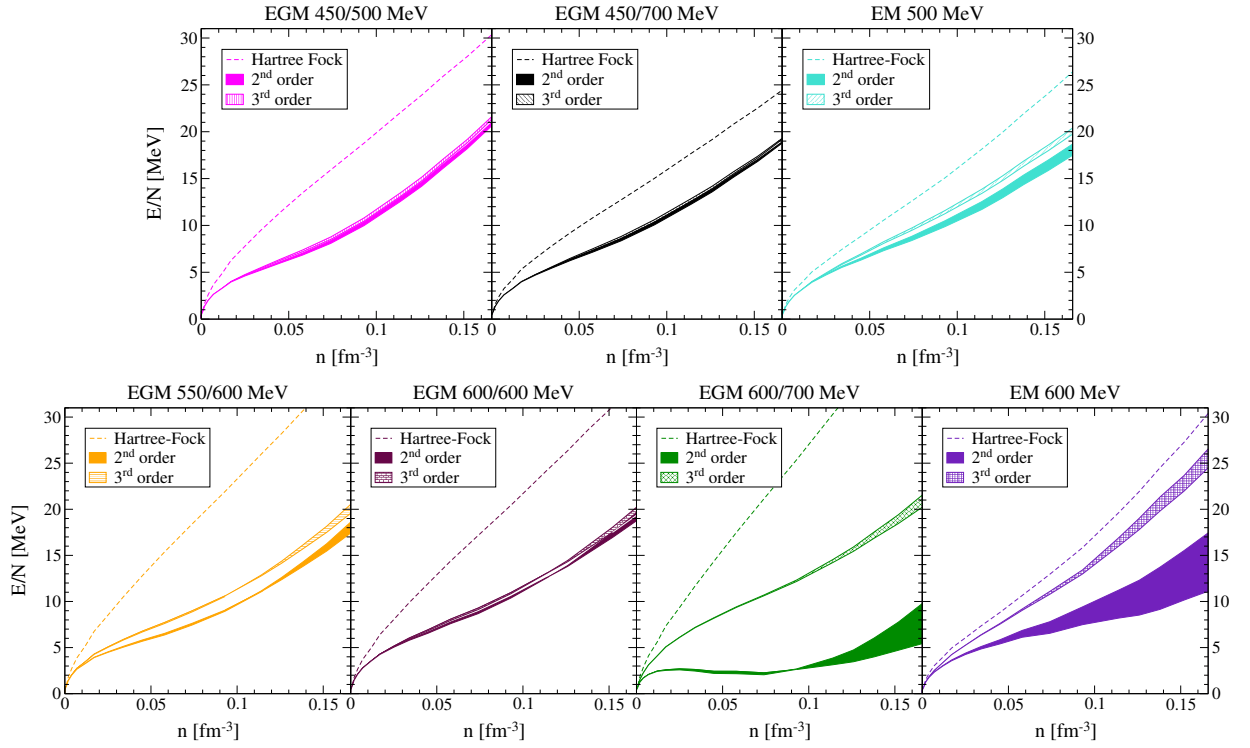


FIG. 4. (Color online) Energy per particle as a function of density for the different $N^3\text{LO}$ NN potentials of Refs. [35–38] and including the leading $N^2\text{LO}$ 3N forces. The dashed lines are Hartree-Fock results only. The filled and shaded bands are second- and third-order energies, respectively, where at each order the band ranges from using a free to a Hartree-Fock spectrum. All calculations are performed for a 3N cutoff $\Lambda = 2.0 \text{ fm}^{-1}$ and low-energy couplings $c_1 = 0.75 \text{ GeV}^{-1}$ and $c_3 = 4.77 \text{ GeV}^{-1}$.

essary condition for the perturbative convergence. The perturbative convergence is a result of effective-range effects [45], which weaken NN interactions at higher momenta, combined with weaker tensor forces among neutrons, and with limited phase space at finite density due to Pauli blocking [25]. For the EM 500 MeV potential the inclusion of the $N^2\text{LO}$ 3N forces decreases the uncertainty estimate from the different single-particle energies, but increases the difference between second and third order. This can be seen comparing Figs. 3 and 4 and is reflected in the uncertainty estimate given in Table III. Since this potential is most commonly used in nuclear structure calculations, we have decided to keep it in our complete $N^3\text{LO}$ calculation, in addition to the lower cutoff $N^3\text{LO}$ EGM 450/500 and 450/700 MeV potentials.

The $N^3\text{LO}$ EGM 550/600 MeV potential is not used in the following calculations because its uncertainty estimate (see Table III) increases by a factor of 3 when the $N^2\text{LO}$ 3N forces are included. This leads to a worse convergence pattern compared to the low-cutoff EGM potentials. For the $N^3\text{LO}$ EGM 600/700 MeV and EM 600 MeV potentials we find the situation unchanged when including 3N forces and, thus, do not use these potentials for the following calculations. Even though the $N^3\text{LO}$ EGM 600/600 MeV potential exhibits a good convergence pattern, we will not use this interaction because it breaks Wigner symmetry at the interaction level (see the discussion of Table I). Finally, we note that our findings for the EM 500 MeV potential are consistent with Ref. [46] (see Fig. 6 therein), where the authors studied this potential at third order employing a Hartree-Fock spectrum.

IV. RESULTS AND DISCUSSION

Next, we present results using the EGM potentials with cutoffs 450/500 and 450/700 MeV and the EM 500 MeV potential. We discuss the individual contributions first and then show the complete $N^3\text{LO}$ results.

A. $N^3\text{LO}$ NN and $N^2\text{LO}$ 3N forces

The $N^3\text{LO}$ NN and $N^2\text{LO}$ 3N forces have been evaluated at the Hartree-Fock level and including second- and third-order contributions. Beyond Hartree Fock, $N^2\text{LO}$ 3N forces are taken into account as density-dependent two-body interactions [4]. The kinetic energy, Hartree-Fock, and individual higher-order interaction contributions for the $N^3\text{LO}$ NN and $N^2\text{LO}$ 3N parts are given in Table IV for different values of Λ and the c_i couplings. Vanishing c_i in the 3N forces correspond to NN forces only. Table IV shows that the dominant higher-order contributions are due to the second-order NN-NN part $E_1^{(2)}$. The second-order NN-3N parts $E_2^{(2)} + E_3^{(2)}$ are of the order of 1 MeV and only larger for the large 3N cutoff. All higher-order contributions with 3N forces are systematically smaller. We emphasize that the $N^2\text{LO}$ 3N contri-

butions beyond Hartree Fock are larger than in Ref. [4], and therefore also the many-body calculation converges more slowly, because the $N^2\text{LO}$ 3N forces are stronger due to the large $N^3\text{LO}$ values of the c_i couplings.

The NN-only energies per particle are 14.7, 12.1, and 12.9 MeV at saturation density for the EGM 450/500, EGM 450/700 MeV, and EM 500 MeV $N^3\text{LO}$ potentials, respectively. Inclusion of 3N forces at $N^2\text{LO}$ adds another 7 ± 1.5 MeV per particle at saturation density (using the larger $N^3\text{LO}$ c_i values, see Table II).

B. $N^3\text{LO}$ 3N and 4N forces

The $N^3\text{LO}$ many-body forces have been evaluated in the Hartree-Fock approximation. We have not calculated higher-order contributions because of their involved structure. The Hartree-Fock approximation is expected to be reliable based on the findings of Ref. [4]. In addition, higher-order contributions with $N^3\text{LO}$ many-body forces are not enhanced by large c_i couplings, and the $N^3\text{LO}$ many-body forces are smaller than at $N^2\text{LO}$, leading to smaller higher-order corrections.

We show the individual contributions of the 3N and 4N forces in Fig. 5. The bands correspond to the cutoff variation $\Lambda = 2 - 2.5 \text{ fm}^{-1}$. In the shorter-range two-pion-exchange-contact and the relativistic corrections 3N forces, three different bands are shown. These correspond to the different NN contacts, C_T and C_S , determined consistently for the different $N^3\text{LO}$ EM/EGM potentials.

The two-pion-exchange 3N forces at $N^3\text{LO}$ yield an energy per particle of -1.5 MeV at saturation density, which is $\sim 1/3$ of the 3N contributions at $N^2\text{LO}$ and sets the natural scale. The two-pion-one-pion-exchange and the pion-ring 3N forces lead to relatively large contributions of -3.5 MeV and $+3.3$ MeV per particle at n_0 , respectively. The contributions of the two-pion-exchange-contact 3N forces range between -2.8 MeV and $+1.3$ MeV per particle at n_0 , depending on the NN potential. In the topologies with relatively large expectation values, the large c_i couplings will enter in many-body forces at $N^4\text{LO}$ [43]. This may reflect important Δ contributions shifted to $N^4\text{LO}$, as discussed above. Finally, the relativistic corrections contribute $-(0.1 - 0.3)$ MeV to the energy per particle at n_0 and are small compared with the other topologies.

As shown in Fig. 6 (second panel) the sum of the $N^3\text{LO}$ 3N contributions yields an energy of $-(3 - 5)$ MeV per particle at saturation density for the EGM potentials and a small contribution of -0.5 MeV for the EM potential. This shows that the $N^3\text{LO}$ 3N contribution can be significant, compared to the $N^2\text{LO}$ 3N energy of 7 ± 1.5 MeV per particle (note that the first panel of Fig. 6 only gives this contribution at the Hartree-Fock level). The relatively large $N^3\text{LO}$ 3N contributions are compensated by the larger $N^3\text{LO}$ c_i values, entering the 3N force at $N^2\text{LO}$. This can be seen in Fig. 6 where the total 3N contribution at $N^3\text{LO}$ (third panel) is compared at the Hartree-

TABLE IV. Contributions from different $N^3\text{LO}$ NN potentials and the leading $N^2\text{LO}$ 3N forces to the neutron-matter energy per particle in MeV at nuclear saturation density. A Hartree-Fock spectrum for the single-particle energies has been used. The 3N force is for different Λ in fm^{-1} and for different c_1, c_3 in GeV^{-1} .

NN potential	c_1/c_3 (3N)	Λ	$E_{\text{kin}}^{(0)}$	$E_{\text{NN}}^{(1)}$	$E_{3\text{N}}^{(1)}$	$E_1^{(2)}$	$E_2^{(2)} + E_3^{(2)}$	$E_4^{(2)}$	$E_1^{(3)}$	$E_2^{(3)} + E_3^{(3)}$	$E_4^{(3)}$
EGM 450/500 MeV	0/0	—	35.93	-13.51	0	-7.88	0	0	0.11	0	0
		2.0	35.93	-13.51	7.95	-8.37	-0.92	-0.22	0.14	0.45	0.03
	-0.75/-4.77	2.5	35.93	-13.51	9.06	-7.94	-3.41	-0.95	0.35	0.32	0.15
		2.0	35.93	-13.51	9.37	-8.47	-1.08	-0.31	0.14	0.55	0.04
	-1.13/-5.51	2.5	35.93	-13.51	10.67	-7.97	-3.98	-1.31	0.39	0.81	0.22
EGM 450/700 MeV	0/0	—	35.93	-19.39	0	-4.49	0	0	0.08	0	0
		2.0	35.93	-19.39	7.95	-4.77	-0.63	-0.22	0.09	0.25	0.02
	-0.75/-4.77	2.5	35.93	-19.39	9.06	-4.52	-2.45	-0.96	0.19	0.40	0.13
		2.0	35.93	-19.39	9.37	-4.83	-0.74	-0.31	0.10	0.31	0.03
	-1.13/-5.51	2.5	35.93	-19.39	10.67	-4.54	-2.87	-1.32	0.21	0.50	0.19
EM 500 MeV	0/0	—	35.93	-17.49	0	-6.71	0	0	1.13	0	0
		2.0	35.93	-17.49	7.95	-7.13	-0.52	-0.19	1.26	0.39	0.02
	-0.75/-4.77	2.5	35.93	-17.49	9.06	-6.84	-2.27	-0.83	1.21	0.96	0.14
		2.0	35.93	-17.49	9.37	-7.21	-0.61	-0.27	1.29	0.47	0.03
	-1.13/-5.51	2.5	35.93	-17.49	10.67	-6.87	-2.67	-1.14	1.23	1.17	0.20

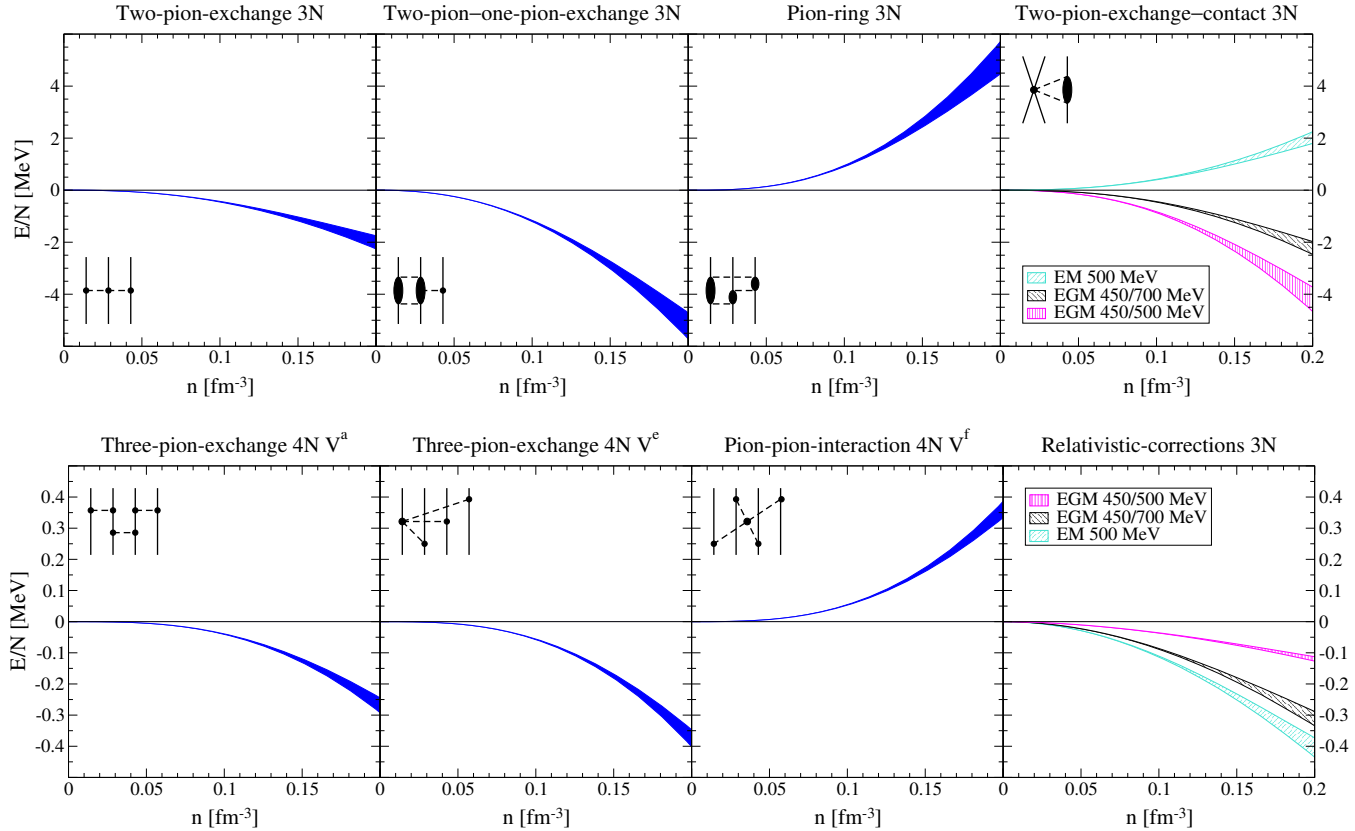


FIG. 5. (Color online) Energy per particle as a function of density for all individual $N^3\text{LO}$ 3N- and 4N-force contributions to neutron matter at the Hartree-Fock level. All bands are obtained by varying the 3N/4N cutoffs $\Lambda = 2 - 2.5 \text{ fm}^{-1}$. For the two-pion-exchange-contact and the relativistic-corrections 3N forces, the different bands correspond to the different NN contacts, C_T and C_S , determined consistently for the $N^3\text{LO}$ EM/EGM potentials. The inset diagram illustrates the 3N/4N force topology of the particular contributions.

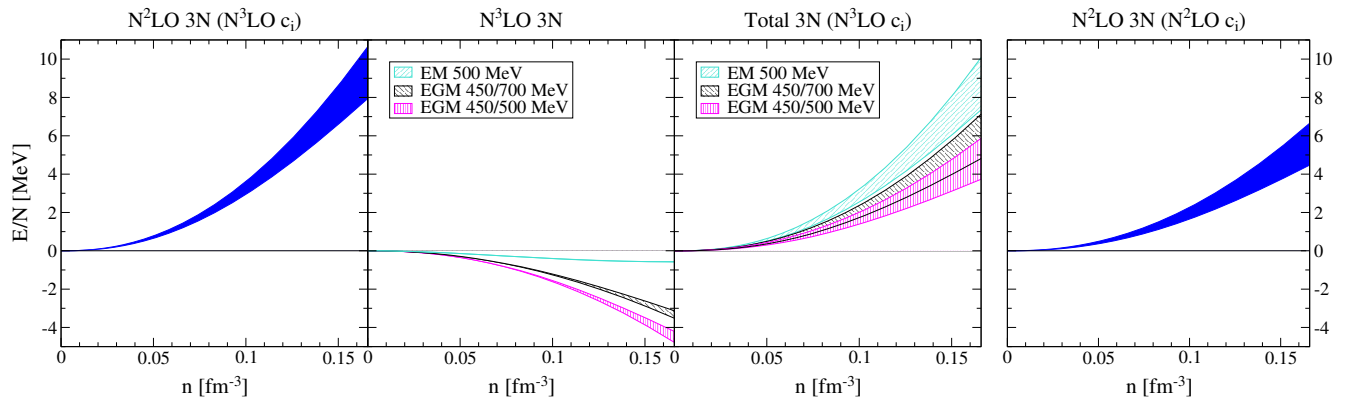


FIG. 6. (Color online) Contributions from 3N forces in the Hartree-Fock approximation at N^2 LO plus N^3 LO (first three panels) in comparison with the 3N contribution in a N^2 LO calculation (fourth panel). The first panel shows the N^2 LO 3N contribution in the N^3 LO calculation, using the N^3 LO values of the c_i couplings, and the second panel gives the N^3 LO 3N contribution. The third panel shows the total 3N contribution at N^3 LO (the sum of the first two panels). This is compared in the fourth panel to the 3N contribution at N^2 LO, using the c_i values recommended for an N^2 LO calculation (see Table II). For the EGM potentials the total 3N contribution at N^3 LO differs by less than 1 MeV compared to the N^2 LO results. However, for the EM potential, the result changes by almost 3 MeV. All bands include the c_i range from Table II and the 3N cutoff variation.

Fock level to the 3N contribution at N^2 LO (fourth panel), which uses the c_i values recommended for an N^2 LO calculation (see Table II). For the EGM potentials the total 3N contribution changes by less than 1 MeV going from N^2 LO to N^3 LO. Because the N^3 LO 3N contribution is small for the EM potential, this results in a difference of about 3 MeV when going from N^2 LO to N^3 LO for the EM case, due to the modified c_i couplings at N^3 LO.

Only three N^3 LO 4N topologies give nonvanishing contributions to neutron matter. We show their results in Fig. 5. The two three-pion-exchange diagrams V^a and V^e are attractive with energies of -0.16 MeV and -0.25 MeV per particle at saturation density. The pion-pion-interaction 4N forces (V^f) are repulsive with 0.22 MeV per particle at n_0 . The latter two diagrams almost cancel each other, such that the total contribution of the leading 4N forces is about -0.18 MeV per particle at n_0 . However, also for the 4N forces additional larger contributions from Δ excitations may arise at N^4 LO [44].

At the Hartree-Fock level, the 3N/4N contributions change by less than 5% if the cutoff is taken to infinity (i.e., $f_R = 1$). However, since we also include N^2 LO 3N forces beyond Hartree Fock, a consistent regulator is required. Finally, we compare our 4N results with those of Refs. [44, 47], which considered only the 4N interactions V^e and V^f and found their sum to be about -11 keV per particle at n_0 . This is in agreement with our results, if we take $f_R = 1$ as in Refs. [44, 47].

C. Complete calculation at N^3 LO

The complete N^3 LO result for neutron matter is shown in Fig. 7, which includes all many-body interactions to N^3 LO [3]. For all shown potentials the uncertainties in

the c_i couplings dominate the width of the bands (compare to the bands in the upper row of Fig. 4).

At saturation density, we obtain for the energy per particle

$$\frac{E}{N}(n_0) = 14.1 - 21.0 \text{ MeV}. \quad (17)$$

This range is based on different NN potentials, a variation of the couplings $c_1 = -(0.75 - 1.13) \text{ GeV}^{-1}$ and $c_3 = -(4.77 - 5.51) \text{ GeV}^{-1}$, and on the 3N/4N-cutoff variation $\Lambda = 2 - 2.5 \text{ fm}^{-1}$. In addition, the uncertainty in the many-body calculation is included, as discussed above.

As shown in Fig. 7, our results are consistent with previous calculations based on RG-evolved NN interactions at N^3 LO and 3N interactions at N^2 LO [4]. These calculations adopted a conservative c_i range but are based on the EM 500 MeV NN potential only, which results in a narrower band compared to the N^3 LO band. In Ref. [3], we compared our results to calculations based on lattice EFT [22] and quantum Monte Carlo at low densities [48], as well as to variational methods [49] and auxiliary field diffusion Monte Carlo [50] based on phenomenological NN and 3N potentials, and found that they are also consistent with the N^3 LO band. However, the latter calculations do not provide theoretical uncertainties.

In Fig. 8 we compare the convergence from N^2 LO to N^3 LO in the same calculational setup. For this comparison, we consider only the EGM potentials with cutoffs 450/500 and 450/700 MeV, since no EM N^2 LO potential is available. This leads to an N^3 LO energy range of $14.1 - 18.4$ MeV per particle at n_0 . For the N^2 LO band in Fig. 8, we have estimated the theoretical uncertainties in the same way and found an energy of $15.5 - 21.4$ MeV per particle at n_0 . The two bands overlap but the range of the band is reduced only by a factor of $2/3$, which is

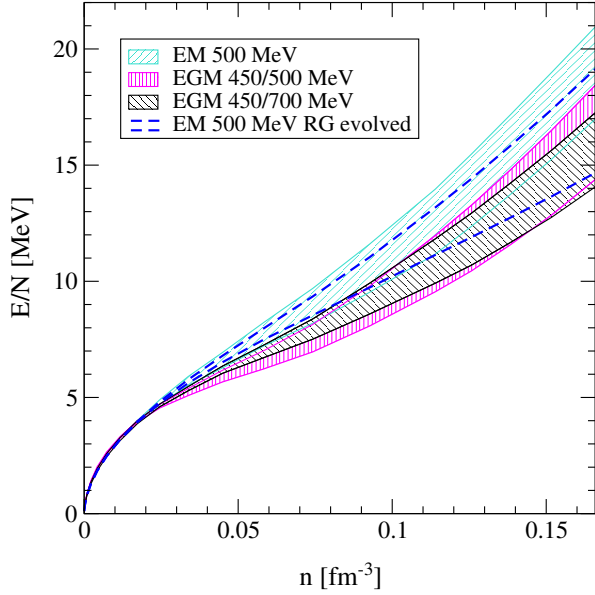


FIG. 7. (Color online) Neutron-matter energy per particle as a function of density including NN, 3N, and 4N forces to N³LO. The three overlapping bands are labeled by the different NN potentials and include uncertainty estimates due to the many-body calculation, the low-energy c_i constants, and by varying the 3N/4N cutoffs (see text for details). For comparison, we show the results for the RG-evolved NN EM 500 MeV potential including only N²LO 3N forces from Ref. [4].

larger than the 1/3 expected from the EFT power counting. We attribute this to Δ effects (as discussed above). This can be improved by including the Δ in chiral EFT explicitly or by going to N⁴LO [43].

Finally, it is important to construct NN potentials at N²LO and N³LO covering the range of the c_i values. At N³LO, we expect that the differences in the c_i can be absorbed partly by Q^4 contact interactions in the fits to NN scattering. In addition, the many-body-calculation uncertainties can be reduced further by including the N³LO many-body forces beyond the Hartree-Fock level.

V. APPLICATIONS

A. Symmetry energy and its density derivative

The symmetry energy S_v and its density derivative L provide important input for astrophysics [51]. To calculate these, we need to extend the neutron-matter energy to asymmetric matter. For the energy per particle ϵ , we follow Ref. [52] and take an expression that includes kinetic energy plus interaction energy that is quadratic in

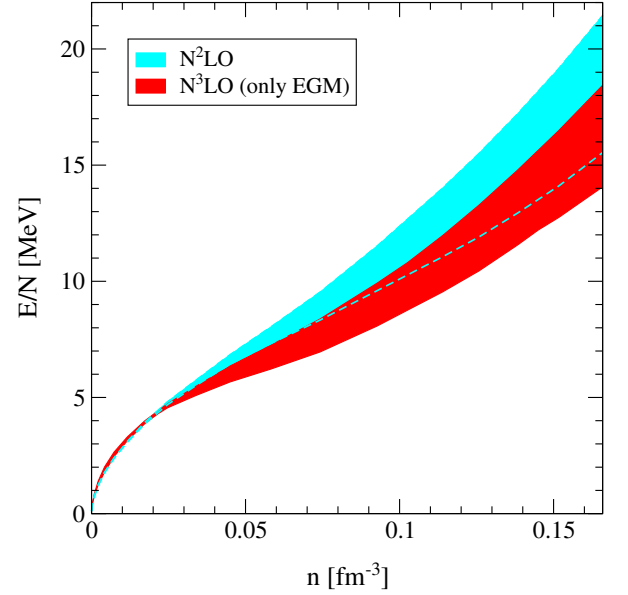


FIG. 8. (Color online) Neutron-matter energy per particle as a function of density at N²LO (upper blue band that extends to the dashed line) and N³LO (lower red band). The bands are based on the EGM NN potentials and include uncertainty estimates as in Fig. 7.

the neutron excess $1 - 2x$, where x is the proton fraction,

$$\epsilon(\bar{n}, x) = T_0 \left[\frac{3}{5} \left[x^{\frac{5}{3}} + (1-x)^{\frac{5}{3}} \right] (2\bar{n})^{\frac{2}{3}} - [(2\alpha - 4\alpha_L)x(1-x) + \alpha_L]\bar{n} + [(2\eta - 4\eta_L)x(1-x) + \eta_L]\bar{n}^{\frac{4}{3}} \right], \quad (18)$$

where $\bar{n} = n/n_0$ and $T_0 = (3\pi^2 n_0/2)^{2/3}/(2m) = 36.84$ MeV is the Fermi energy of symmetric nuclear matter at saturation density. The parameters $\alpha = 5.87$ and $\eta = 3.81$ are determined through fits to the empirical saturation point of nuclear matter, and α_L and η_L through fits to the neutron-matter results of Fig. 7 (for details on this strategy, see Ref. [52]). Equation (18) provides very good fits to the N³LO energy band.

We can then calculate the symmetry energy

$$S_v(n) = \frac{1}{8} \frac{\partial^2 \epsilon(\bar{n}, x)}{\partial x^2} \Big|_{\bar{n}=1, x=1/2}, \quad (19)$$

TABLE V. Ranges for the symmetry energy S_v and its density derivative L at nuclear saturation density.

	range
Symmetry energy $S_v(n_0)$	28.9 – 34.9 MeV
Density derivative $L(n_0)$	43.0 – 66.6 MeV

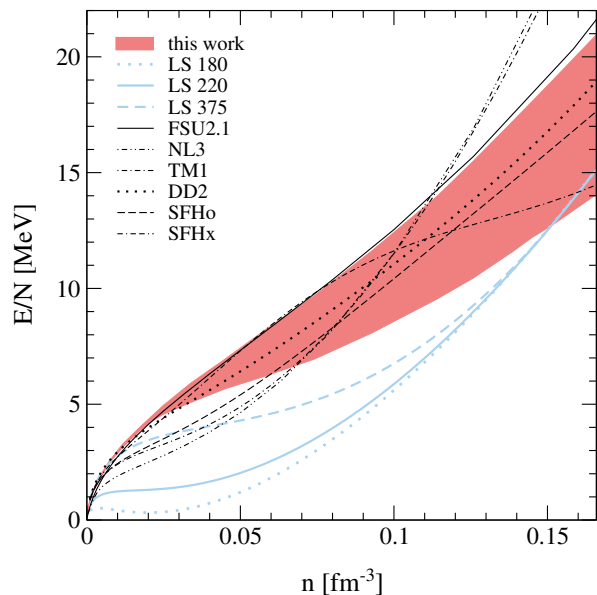


FIG. 9. (Color online) Comparison of the neutron-matter energy at $N^3\text{LO}$ of Fig. 7 (red band) with equations of state for core-collapse supernova simulations provided by Lattimer-Swesty (LS [55] with different incompressibilities, 180, 220, and 375 MeV), G. Shen (FSU2.1, NL3 [61]), Hempel (TM1, SFHo, SFHx [62]), and Typel (DD2 [56]).

and its density derivative

$$L(n) = \frac{3}{8} \frac{\partial^3 \epsilon(\bar{n}, x)}{\partial \bar{n} \partial x^2} \bigg|_{\bar{n}=1, x=1/2}. \quad (20)$$

The L parameter basically determines the pressure of neutron matter. In addition, because the expression (18) is fit to the empirical saturation point (with small uncertainties), the symmetry energy and its density derivative at n_0 and their theoretical uncertainties are essentially determined by the neutron-matter results.

The predicted ranges for S_v and L at saturation density are given in Table V. In Ref. [3], we have shown that S_v and L are also correlated and overlap with the results for RG-evolved NN interactions with $N^2\text{LO}$ 3N forces [51, 52], but, due to the additional density dependencies from $N^3\text{LO}$ many-body forces, this correlation is not as tight. The S_v and L ranges are also in very good agreement with experimental constraints from nuclear masses [53] and from the dipole polarizability of ^{208}Pb [54] (see also Refs. [3, 51]).

B. Constraints for supernova equations of state and neutron stars

The neutron-matter results also provide constraints for the nuclear equation of state. Here we focus on comparisons to equations of state for core-collapse supernova

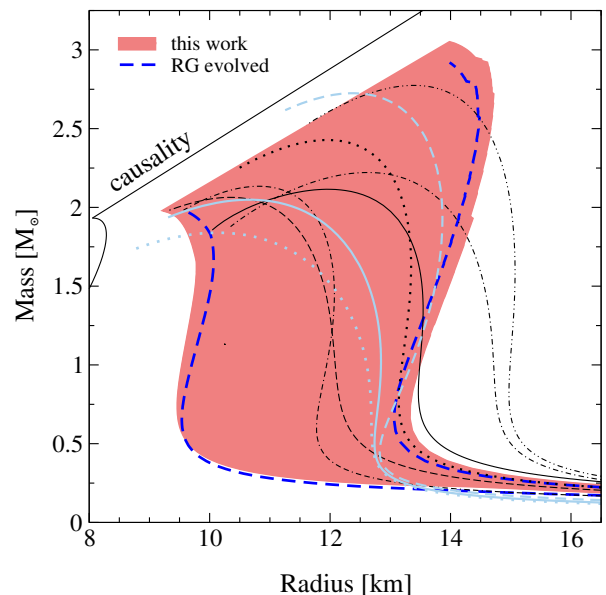


FIG. 10. (Color online) Constraints on the mass-radius diagram of neutron stars based on our neutron-matter results at $N^3\text{LO}$ following Ref. [52] for the extension to neutron-star matter and to high densities (red band), in comparison to the constraints from calculations based on RG-evolved NN interactions (thick dashed blue lines) [52]. We also show the mass-radius relations obtained from the equations of state for core-collapse supernova simulations shown in Fig. 9 [55, 57–60, 64, 65]. The legend for the thin lines is as described in the caption to Fig. 9.

simulations. In Fig. 9, we compare the $N^3\text{LO}$ neutron-matter band (red band) to the Lattimer-Swesty (LS) equation of state [55], which is most commonly used in simulations, and to different relativistic mean-field-theory equations of state based on the density functionals DD2 [56], FSU2.1 [57], NL3 [58], SFHo, SFHx [59], and TM1 [60]. At low densities only the DD2, FSU2.1, and SFHx equations of state are consistent with the $N^3\text{LO}$ neutron-matter band. The other supernova equations of state underestimate the energy for densities below $\sim 0.5n_0$ and even at higher density in the LS cases. This density range covers the outer regions of the (proto-) neutron star, where also protons, nuclei, and electrons are relevant. Nevertheless, the deficiencies in the nuclear interactions of these equations of state will also affect the chemical potentials and the neutrino response. Around saturation density, the LS and SFHo equations of state become consistent with the $N^3\text{LO}$ band. We also find that the NL3 and TM1 equations of state have a too strong density dependence, which leads to unnaturally large S_v and L values. In addition, Fig. 9 exhibits a strange density dependence of SFHx.

Next, we use the $N^3\text{LO}$ neutron-matter results to provide constraints for the structure of neutron stars. We follow Ref. [52] for incorporating β equilibrium and for the extension to high densities using piecewise polytropes

that are constrained by causality and by the requirement to support a $1.97 \pm 0.04 M_\odot$ neutron star [63], the heaviest precisely measured neutron star to date. The resulting constraints on the neutron star mass-radius diagram are shown in Fig. 10 by the red band. This band represents an envelope of a large number of individual equations of state reflecting the uncertainties in the $N^3\text{LO}$ neutron-matter calculation and in the polytropic extensions to high densities [52]. Figure 10 confirms the predicted radius range of Ref. [52] of $9.7 - 13.9 \text{ km}$ for a $1.4 M_\odot$ neutron star. The largest supported neutron star mass is found to be $3.1 M_\odot$, with a corresponding radius of about 14 km . We also find very good agreement with the mass-radius constraints from the neutron-matter calculations based on RG-evolved NN interactions with $N^2\text{LO}$ 3N forces [52], which are shown by the thick dashed blue lines in Fig. 10.

In addition, we show in Fig. 10 the mass-radius relations obtained from equations of state for core-collapse supernova simulations [55, 57–60, 64, 65]. The inconsistency in Fig. 9 of many of the equations of state with the $N^3\text{LO}$ neutron-matter band at low densities results in a large spread of very low mass/large radius neutron stars, where the red band is considerably narrower in Fig. 10 (note that the red band includes a standard crust equation of state below $0.5 n_0$ [52]). For typical neutron stars, our calculations rule out the NL3 and TM1 equations of state, which produce too-large radii. Finally, we emphasize that these constraints not only are important for neutron star structure and for the supernova equation of state but also provide nuclear physics constraints for the gravitational wave signal in neutron star mergers [66, 67].

VI. FIRST ESTIMATE FOR SYMMETRIC NUCLEAR MATTER

We present first results for the $N^3\text{LO}$ many-body forces in symmetric nuclear matter in the Hartree-Fock approximation. However, we emphasize that these results should be considered as a preview and to show their importance, because it is crucial to include contributions beyond the Hartree-Fock level [34]. Such calculations can also be facilitated by a similarity RG evolution of NN and 3N forces [68, 69] in order to improve the convergence of the many-body calculation.

The energy per particle of symmetric matter is evaluated as in Sec. III A summing also over both isospin states [see Eq. (B1)]. In Appendix B, the expressions for the $N^3\text{LO}$ 3N- and 4N-interaction matrix elements are given in detail. Our results for the individual contributions from $N^3\text{LO}$ many-body forces are shown in Fig. 11. Compared to the neutron-matter results, the individual contributions are larger in magnitude in symmetric matter, requiring calculations beyond the Hartree-Fock level. However, the bands from cutoff variation are narrower, because the Fermi momentum corresponding to saturation density is lower in symmetric matter.

For the two-pion-exchange $N^3\text{LO}$ 3N forces the energy is small, with 0.24 MeV per particle at n_0 due to cancellations among the individual parts in symmetric matter. The other 3N topologies are large and attractive: the two-pion-one-pion-exchange and the pion-ring 3N interactions give energies of -6.5 MeV and -3.6 MeV per particle at n_0 , respectively. The contribution of the two-pion-exchange-contact 3N interaction ranges from -7.0 MeV to $+3.4 \text{ MeV}$, depending on the NN potential. As expected from our neutron-matter results, the large 3N contributions in these topologies can be attributed to the physics from Δ excitations, which will lead to large c_i contributions at $N^4\text{LO}$ in these topologies (or at $N^3\text{LO}$ in Δ -full chiral EFT). As in neutron matter, the contributions from relativistic-corrections 3N forces are small with $-(0.24 - 0.39) \text{ MeV}$ per particle at n_0 .

Since nuclear saturation is a result of cancellation effects of large energy contributions [34], the increased strengths of the c_i couplings at $N^3\text{LO}$ compared to $N^2\text{LO}$ is expected to play an important role for predictions of symmetric matter. Furthermore, in contrast to neutron matter, we find that the total $N^3\text{LO}$ 3N contribution at the Hartree-Fock level depends more strongly on the NN potentials used: For the EM 500 MeV potential, we find -7 MeV per particle at n_0 , whereas for the EGM potentials, we find $-(15 - 17) \text{ MeV}$. To understand this better, improved NN potential fits (following Ref. [70]) and also those for different c_i couplings will be important. These $N^3\text{LO}$ energies should be compared with a total $N^2\text{LO}$ 3N energy at the Hartree-Fock level of the order of 15 MeV per particle at n_0 , using the large $N^3\text{LO}$ c_i values (see Table II and accordingly chosen $c_4 = 3.34 - 3.71 \text{ GeV}^{-1}$ [43]) and typical c_D , c_E values [25]. All these findings show that including $N^3\text{LO}$ 3N contributions beyond the Hartree-Fock level will be crucial.

Figure 11 also shows our results for the individual $N^3\text{LO}$ 4N-force contributions in symmetric matter. The long-range three-pion-exchange 4N interactions V^a and V^e are attractive with energies -0.32 MeV and -0.39 MeV per particle at n_0 , respectively; while the V^c interaction is repulsive with 0.21 MeV per particle at n_0 . The pion-pion-interaction 4N force V^f also gives a repulsive contribution of 0.33 MeV per particle at n_0 . The shorter-range parts V^k , V^l , and V^n contain one or two spin-dependent NN contact interactions and depend on C_T . The two midrange topologies involving only one NN contact (V^k and V^l) almost cancel against each other (-0.11 to $+0.05 \text{ MeV}$ per particle at n_0 , depending on the NN potential, and -0.05 to $+0.10 \text{ MeV}$, respectively). The shortest-range topology with two NN contacts (V^n) contributes even less (-0.06 to -0.01 MeV per particle at n_0). In total, the leading 4N forces give an attractive contribution of $-(0.18 - 0.23) \text{ MeV}$ per particle at n_0 , with a strong density dependence $\sim n^3$.

As a check, we can compare our results to the studies of the V^e and V^f 4N forces of Refs. [44, 47], which obtained a contribution to the energy per particle of -53 keV at n_0 .

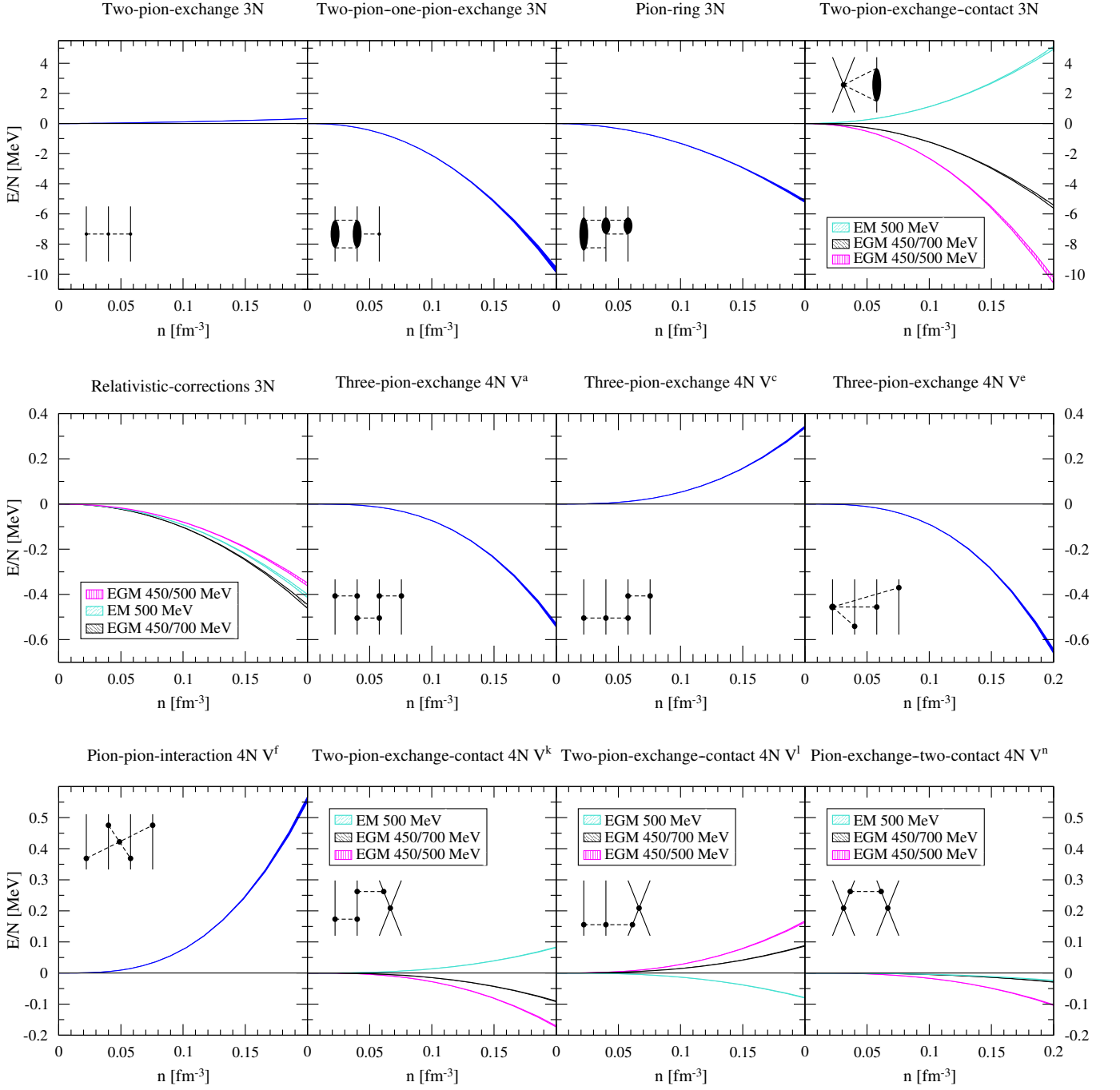


FIG. 11. (Color online) Energy per particle versus density for all individual $N^3\text{LO}$ 3N- and 4N-force contributions to symmetric nuclear matter at the Hartree-Fock level. All bands are obtained by varying the 3N/4N cutoff $\Lambda = 2 - 2.5 \text{ fm}^{-1}$. For the two-pion-exchange-contact, the relativistic-corrections 3N forces, and the short-range 4N forces, the different bands correspond to the different NN contacts, C_T and C_S , determined consistently for the $N^3\text{LO}$ EM/EGM potentials. The inset diagram illustrates the 3N/4N force topology of the particular contribution.

This is in agreement with our result for the sum of these two topologies: $-(56 \pm 2) \text{ keV}$, where the small difference is due to $f_R = 1$ in Refs. [44, 47]. So far only the leading 4N forces have been derived completely. Recently, Kaiser studied Δ contributions to 4N forces [44], which enter at

$N^4\text{LO}$ in Δ -less chiral EFT. Similarly to the $N^3\text{LO}$ versus $N^2\text{LO}$ 3N forces, these contributions are enhanced by the large c_i values, and Kaiser found for these partial $N^4\text{LO}$ 4N contributions a larger energy of $\sim 2 \text{ MeV}$ per particle at saturation density.

Finally, we compare our results for symmetric matter with first calculations of the 4N contributions to the ${}^4\text{He}$ ground-state energy. These were studied in Ref. [71] perturbatively based on the same N^3LO 4N forces. We agree with the sign of the 4N contributions for all topologies and obtain a similar total energy correction when taking a density $\sim n_0/3$. Also, the estimate of Ref. [72] for the V^e 4N contribution to the ${}^4\text{He}$ ground-state energy gave -18 keV per particle, which is of the same order as our results at $\sim n_0/3$.

VII. SUMMARY AND OUTLOOK

We have presented details and additional results of the first complete N^3LO calculation of the neutron-matter energy based on chiral EFT NN, 3N, and 4N interactions [3]. Our results for the energy per particle at saturation density give a range of $14.1 - 21\text{ MeV}$, which includes uncertainties from different NN potentials, from the c_1 and c_3 couplings in 3N forces (these dominate), from varying the cutoff in many-body forces, and from the uncertainties in the perturbative many-body expansion around Hartree Fock. For more systematic studies, it will be important to develop NN potentials that explore the different c_i couplings.

We have found large contributions to the energy from N^3LO 3N forces in topologies where Δ excitations are important. Therefore, an improved EFT convergence is expected in chiral EFT with explicit Δ degrees of freedom. In contrast, contributions from the leading 4N forces are found to be small (see also Refs. [44, 47]). We have presented a first estimate for the N^3LO many-body contributions to the energy of symmetric nuclear matter, where also large N^3LO 3N forces and small leading 4N forces are found. Our results for symmetric matter show that the inclusion of N^3LO 3N forces will be important in nuclear structure calculations, and that it is crucial to go

beyond the Hartree-Fock approximation.

Recently, first Quantum Monte Carlo calculations with chiral EFT interactions are providing nonperturbative benchmarks for neutron matter and validate the perturbative expansion for chiral NN potentials with low cut-offs [28]. Extending these calculations to 3N forces and N^3LO will be important. In addition, the many-body uncertainties can be reduced in the future by a similarity RG evolution of NN and 3N forces [68, 69], which improves the many-body convergence and will also enable studies with the chiral NN interactions, which were found to be nonperturbative in the present calculations.

In addition, we have discussed the impact of our results for astrophysics: The predicted ranges for the symmetry energy S_v and its density derivative L are $S_v = 28.9 - 34.9\text{ MeV}$ and $L = 43.0 - 66.6\text{ MeV}$, which are consistent with recent experimental constraints [51, 53, 54]. Many of the equations of state for core-collapse supernova simulations were found to be inconsistent with the N^3LO neutron-matter band. By extending our neutron-matter results to neutron-star matter and to high densities, we confirm the predicted radius range of $9.7 - 13.9\text{ km}$ for a $1.4 M_\odot$ neutron star [52] and find a maximal neutron star mass of $3.1 M_\odot$.

ACKNOWLEDGMENTS

We thank E. Epelbaum, R. J. Furnstahl, M. Hempel, N. Kaiser, A. Kleiner, H. Krebs, J. M. Lattimer, C. J. Pethick, and G. Shen for discussions. This work was supported by the Helmholtz Alliance Program of the Helmholtz Association, contract HA216/EMMI “Extremes of Density and Temperature: Cosmic Matter in the Laboratory”, by the ERC Grant No. 307986 STRONGINT, the DFG through Grant SFB 634, and by NSF Grant No. PHY-1002478.

Appendix A: N^3LO neutron-matter matrix elements

In this appendix we present the 3N and 4N matrix elements defined as

$$\langle V_{AN} \rangle = \frac{1}{A!} \sum_{\sigma_1, \dots, \sigma_A} \langle 1 \cdots A | \mathcal{A}_A \sum_{i_1 \neq \dots \neq i_A} V_{AN}(i_1, \dots, i_A) | 1 \cdots A \rangle, \quad (\text{A1})$$

entering the neutron-matter Hartree-Fock calculation [see Eq. (2)] of the N^3LO many-body forces.

We use the short-hand notation for the momentum transfer $\mathbf{k}_{ij} = \mathbf{k}_i - \mathbf{k}_j$, $\mathbf{k}_{(ij)(kl)} = \mathbf{k}_{ij} + \mathbf{k}_{kl}$ and $\mathbf{P}_{ij} = \frac{\mathbf{k}_i + \mathbf{k}_j}{2}$, and pion propagators $K_{ij} = k_{ij}^2 + m_\pi^2$ and $K_{(ij)(kl)} = k_{(ij)(kl)}^2 + m_\pi^2$.

1. Two-pion-exchange 3N

$$\begin{aligned} \langle V_{3N}^{2\pi} \rangle = & \frac{g_A^2}{f_\pi^4} \left(-2\delta c_1 m_\pi^2 \left[\frac{\mathbf{k}_{12} \cdot \mathbf{k}_{23}}{K_{12} K_{23}} + \frac{k_{12}^2}{K_{12}^2} \right] + \delta c_3 \left[\frac{(\mathbf{k}_{12} \cdot \mathbf{k}_{23})^2}{K_{12} K_{23}} - \frac{k_{12}^4}{K_{12}^2} \right] \right) \\ & + k_{13}^2 F_{2\pi,1}^{(4)}(-\mathbf{k}_{13}, \mathbf{k}_{13}) - \mathbf{k}_{12} \cdot \mathbf{k}_{13} F_{2\pi,1}^{(4)}(-\mathbf{k}_{12}, \mathbf{k}_{13}), \end{aligned} \quad (\text{A2})$$

with shifts in the low-energy couplings $\delta c_1 = -0.13 \text{ GeV}^{-1}$ and $\delta c_3 = 0.89 \text{ GeV}^{-1}$ (see Ref. [30]) and the function

$$\begin{aligned} F_{2\pi,1}^{(4)}(\mathbf{q}_1, \mathbf{q}_2) = & \frac{3g_A^4}{32\pi f_\pi^6 (q_1^2 + m_\pi^2)(q_2^2 + m_\pi^2)} \left[m_\pi(m_\pi^2 + 3q_1^2 + 3q_2^2 + 4\mathbf{q}_1 \cdot \mathbf{q}_2) \right. \\ & \left. + (2m_\pi^2 + q_1^2 + q_2^2 + 2\mathbf{q}_1 \cdot \mathbf{q}_2)(3m_\pi^2 + 3q_1^2 + 3q_2^2 + 4\mathbf{q}_1 \cdot \mathbf{q}_2) A(|\mathbf{q}_1 + \mathbf{q}_2|) \right], \end{aligned} \quad (\text{A3})$$

where $A(q) = 1/(2q) \arctan[q/(2m_\pi)]$ denotes the loop function [30].

2. Two-pion-one-pion-exchange 3N

$$\begin{aligned} \langle V_{3N}^{2\pi 1\pi} \rangle = & 4 \left[F_1(k_{12}) \frac{(\mathbf{k}_{12} \cdot \mathbf{k}_{13})^2}{K_{13}} - F_2(k_{12}) \frac{\mathbf{k}_{12} \cdot \mathbf{k}_{13}}{K_{13}} - F_3(0) \frac{k_{23}^2}{K_{23}} + F_3(k_{12}) \frac{k_{13}^2}{K_{13}} - F_7(0) \frac{k_{23}^2}{K_{23}} \right. \\ & \left. + F_4(k_{12}) \frac{(\mathbf{k}_{12} \cdot \mathbf{k}_{13})^2}{K_{13}} + F_5(k_{12}) \frac{k_{13}^2}{K_{13}} - F_6(k_{12}) \frac{\mathbf{k}_{12} \cdot \mathbf{k}_{13}}{K_{13}} + F_7(k_{12}) \frac{k_{13}^2}{K_{13}} \right], \end{aligned} \quad (\text{A4})$$

with structure functions $F_1(q)$ to $F_7(q)$ defined in Eqs. (2.17)–(2.20) of Ref. [30].

3. Pion-ring 3N

$$\begin{aligned} \langle V_{3N}^{\text{ring}} \rangle = & 4 \left[-3 R_1(\mathbf{k}_{12}, 0) + 3 R_1(\mathbf{k}_{12}, \mathbf{k}_{23}) - k_{12}^2 R_2(\mathbf{k}_{12}, 0) + k_{12}^2 R_2(\mathbf{k}_{12}, \mathbf{k}_{23}) + \mathbf{k}_{12} \cdot \mathbf{k}_{23} R_3(\mathbf{k}_{12}, \mathbf{k}_{23}) \right. \\ & + \mathbf{k}_{12} \cdot \mathbf{k}_{23} R_4(\mathbf{k}_{12}, \mathbf{k}_{23}) + k_{23}^2 R_5(\mathbf{k}_{12}, \mathbf{k}_{23}) + 2R_6(0, 0) - R_6(\mathbf{k}_{12}, 0) - R_6(0, \mathbf{k}_{12}) - R_6(-\mathbf{k}_{12}, \mathbf{k}_{12}) \\ & + R_6(\mathbf{k}_{12}, \mathbf{k}_{23}) - k_{12}^2 R_7(-\mathbf{k}_{12}, \mathbf{k}_{12}) + k_{12}^2 R_7(\mathbf{k}_{12}, \mathbf{k}_{23}) + k_{12}^2 R_8(-\mathbf{k}_{12}, \mathbf{k}_{12}) + \mathbf{k}_{12} \cdot \mathbf{k}_{23} R_8(\mathbf{k}_{12}, \mathbf{k}_{23}) \\ & + k_{12}^2 R_9(-\mathbf{k}_{12}, \mathbf{k}_{12}) + \mathbf{k}_{12} \cdot \mathbf{k}_{23} R_9(\mathbf{k}_{12}, \mathbf{k}_{23}) - 3R_{10}(-\mathbf{k}_{12}, \mathbf{k}_{12}) + 3R_{10}(\mathbf{k}_{12}, \mathbf{k}_{23}) + 2S_1(0, 0) \\ & - S_1(\mathbf{k}_{12}, 0) - S_1(0, \mathbf{k}_{12}) - S_1(-\mathbf{k}_{12}, \mathbf{k}_{12}) + S_1(\mathbf{k}_{12}, \mathbf{k}_{23}) - k_{12}^2 S_2(-\mathbf{k}_{12}, \mathbf{k}_{12}) + k_{12}^2 S_2(\mathbf{k}_{12}, \mathbf{k}_{23}) \\ & + k_{12}^2 S_3(-\mathbf{k}_{12}, \mathbf{k}_{12}) + \mathbf{k}_{12} \cdot \mathbf{k}_{23} S_3(\mathbf{k}_{12}, \mathbf{k}_{23}) + k_{12}^2 S_4(-\mathbf{k}_{12}, \mathbf{k}_{12}) + \mathbf{k}_{12} \cdot \mathbf{k}_{23} S_4(\mathbf{k}_{12}, \mathbf{k}_{23}) \\ & \left. - k_{12}^2 S_5(-\mathbf{k}_{12}, \mathbf{k}_{12}) + k_{23}^2 S_5(\mathbf{k}_{12}, \mathbf{k}_{23}) - 3S_6(-\mathbf{k}_{12}, \mathbf{k}_{12}) + 3S_6(\mathbf{k}_{12}, \mathbf{k}_{23}) \right], \end{aligned} \quad (\text{A5})$$

where the structure functions R_i and S_i are defined in Eqs. (A2) and (A7) of Ref. [30].

4. Two-pion-exchange-contact 3N

$$\langle V_{3N}^{2\pi\text{-cont}} \rangle = -\frac{g_A^2}{2\pi f_\pi^4} C_T \left(g_A^2 \left[\frac{3m_\pi}{4} + \frac{m_\pi^3}{4m_\pi^2 + k_{12}^2} - 2(2m_\pi^2 + k_{12}^2)A(k_{12}) \right] - \left[\frac{m_\pi}{2} - (2m_\pi^2 + k_{12}^2)A(k_{12}) \right] \right). \quad (\text{A6})$$

5. Relativistic-corrections 3N

$$\begin{aligned} \langle V_{3N}^{1/m} \rangle = 2 & \left[k_{12}^2 F_{1/m}^1(\mathbf{k}_{12}, \mathbf{k}_{12}) + \mathbf{k}_{12} \cdot \mathbf{k}_{23} F_{1/m}^1(\mathbf{k}_{12}, \mathbf{k}_{23}) - (\mathbf{k}_{12} \times \mathbf{k}_{23})^2 F_{1/m}^2(-\mathbf{k}_{12}, \mathbf{k}_{13}, \mathbf{P}_{12}, \mathbf{P}_{23}) \right. \\ & + k_{12}^2 F_{1/m}^3(\mathbf{k}_{12}, \mathbf{k}_{12}) + \mathbf{k}_{12} \cdot \mathbf{k}_{23} F_{1/m}^3(\mathbf{k}_{12}, \mathbf{k}_{23}) - (\mathbf{k}_{12} \times \mathbf{k}_{13}) \cdot (\mathbf{k}_{12} \times \mathbf{P}_{23}) F_{1/m}^4(\mathbf{k}_{12}, \mathbf{k}_{13}) \\ & - (\mathbf{k}_{12} \times \mathbf{k}_{13}) \cdot (\mathbf{k}_{12} \times \mathbf{P}_{13}) F_{1/m}^5(\mathbf{k}_{12}, \mathbf{k}_{13}) + k_{12}^2 F_{1/m}^6(\mathbf{k}_{12}, \mathbf{k}_{23}) - k_{12}^2 F_{1/m}^7(\mathbf{k}_{12}, -\mathbf{k}_{12}) \\ & \left. + k_{12}^2 F_{1/m}^7(\mathbf{k}_{12}, \mathbf{k}_{23}) - k_{12}^2 F_{1/m}^8(\mathbf{k}_{12}, \mathbf{P}_{12}, \mathbf{P}_{23}) - k_{12}^2 F_{1/m}^9(k_{12}) + k_{12}^2 F_{1/m}^{10}(k_{12}) + k_{12}^2 F_{1/m}^{11}(k_{12}) \right], \quad (\text{A7}) \end{aligned}$$

with

$$F_{1/m}^1(\mathbf{q}_1, \mathbf{q}_2) = -\frac{g_A^4}{16mf_\pi^4} \frac{(1 - 2\bar{\beta}_8)(\mathbf{q}_1 \cdot \mathbf{q}_2)^2}{(q_1^2 + m_\pi^2)^2(q_2^2 + m_\pi^2)}, \quad (\text{A8})$$

$$F_{1/m}^2(\mathbf{q}_1, \mathbf{q}_2, \mathbf{q}_3, \mathbf{q}_4) = \frac{g_A^4}{8mf_\pi^4} \frac{(1 - 2\bar{\beta}_8)\mathbf{q}_1 \cdot \mathbf{q}_4 + (1 + 2\bar{\beta}_8)\mathbf{q}_1 \cdot \mathbf{q}_3}{(q_1^2 + m_\pi^2)^2(q_2^2 + m_\pi^2)}, \quad (\text{A9})$$

$$F_{1/m}^3(\mathbf{q}_1, \mathbf{q}_2) = -\frac{g_A^4}{16mf_\pi^4} \frac{(2\bar{\beta}_9 - 1)q_1^2}{(q_1^2 + m_\pi^2)(q_2^2 + m_\pi^2)} = -F_{1/m}^4(\mathbf{q}_1, \mathbf{q}_2) \frac{q_1^2}{2} = -F_{1/m}^5(\mathbf{q}_1, \mathbf{q}_2) \frac{q_1^2(2\bar{\beta}_9 - 1)}{2(2\bar{\beta}_9 + 1)}, \quad (\text{A10})$$

$$F_{1/m}^6(\mathbf{q}_1, \mathbf{q}_2) = \frac{g_A^2}{4mf_\pi^2} C_S \frac{(1 - 2\bar{\beta}_8)\mathbf{q}_1 \cdot \mathbf{q}_2}{(q_1^2 + m_\pi^2)^2} = F_{1/m}^7(\mathbf{q}_1, \mathbf{q}_2) \frac{C_S}{C_T}, \quad (\text{A11})$$

$$F_{1/m}^8(\mathbf{q}_1, \mathbf{q}_2, \mathbf{q}_3) = \frac{g_A^2}{mf_\pi^2} C_T \frac{(1 - 2\bar{\beta}_8)\mathbf{q}_1 \cdot \mathbf{q}_3 + (1 + 2\bar{\beta}_8)\mathbf{q}_1 \cdot \mathbf{q}_2}{(q_1^2 + m_\pi^2)^2}, \quad (\text{A12})$$

$$F_{1/m}^9(q) = \frac{g_A^2}{8mf_\pi^2} C_S \frac{2\bar{\beta}_9 - 1}{q^2 + m_\pi^2} = F_{1/m}^{10}(q) \frac{C_S}{C_T} = F_{1/m}^{11}(q) \frac{C_S}{2C_T}. \quad (\text{A13})$$

6. Three-pion-exchange and pion-interaction 4N

$$\begin{aligned} \langle V_{4N}^a \rangle = & -\frac{g_A^6}{8f_\pi^6} \left(\left[(\mathbf{k}_1 \times \mathbf{k}_2) \cdot \mathbf{k}_{34} + (\mathbf{k}_3 \times \mathbf{k}_4) \cdot \mathbf{k}_{12} \right]^2 \left[\frac{1}{K_{14}K_{(14)(23)}^2K_{24}} + \frac{1}{K_{12}K_{14}^2K_{34}} - \frac{1}{K_{12}K_{13}^2K_{14}} \right] \right. \\ & + \frac{k_{14}^2(\mathbf{k}_{14} \times \mathbf{k}_{(14)(23)})^2}{K_{14}^2K_{(14)(23)}^2} - \frac{\mathbf{k}_{14} \cdot \mathbf{k}_{24}(\mathbf{k}_{(14)(23)} \times \mathbf{k}_{14}) \cdot (\mathbf{k}_{(14)(23)} \times \mathbf{k}_{24})}{K_{14}K_{(14)(23)}^2K_{24}} \\ & \left. + \frac{\mathbf{k}_{12} \cdot \mathbf{k}_{34}(\mathbf{k}_{14} \times \mathbf{k}_{12}) \cdot (\mathbf{k}_{14} \times \mathbf{k}_{34})}{K_{12}K_{14}^2K_{34}} - \frac{\mathbf{k}_{12} \cdot \mathbf{k}_{14}(\mathbf{k}_{13} \times \mathbf{k}_{12}) \cdot (\mathbf{k}_{13} \times \mathbf{k}_{14})}{K_{12}K_{13}^2K_{14}} \right), \quad (\text{A14}) \end{aligned}$$

$$\begin{aligned} \langle V_{4N}^e \rangle = & \frac{g_A^4}{16f_\pi^6} \left[-2 \frac{k_{24}^2}{K_{13}K_{24}^2} \mathbf{k}_{13} \cdot (\mathbf{k}_{13} + \mathbf{k}_{24}) - \frac{\mathbf{k}_{13} \cdot \mathbf{k}_{24}}{K_{13}K_{23}K_{24}} \mathbf{k}_{23} \cdot (\mathbf{k}_{13} + \mathbf{k}_{24}) + 2 \frac{\mathbf{k}_{13} \cdot \mathbf{k}_{34}}{K_{13}K_{24}K_{34}} \mathbf{k}_{24} \cdot \mathbf{k}_{14} \right. \\ & \left. + 2 \frac{\mathbf{k}_{23} \cdot \mathbf{k}_{24}}{K_{13}K_{23}K_{24}} \mathbf{k}_{13} \cdot (\mathbf{k}_{13} + \mathbf{k}_{24}) + 2 \frac{\mathbf{k}_{23} \cdot \mathbf{k}_{14}}{K_{14}K_{23}K_{34}} \mathbf{k}_{34} \cdot \mathbf{k}_{13} + 2 \frac{\mathbf{k}_{12} \cdot \mathbf{k}_{24}}{K_{12}K_{24}K_{34}} \mathbf{k}_{34} \cdot \mathbf{k}_{23} \right], \quad (\text{A15}) \end{aligned}$$

$$\begin{aligned} \langle V_{4N}^f \rangle = & \frac{g_A^4}{32f_\pi^6} \left[(m_\pi^2 + 2K_{(12)(34)}) \frac{k_{12}^2 k_{34}^2}{K_{12}^2 K_{34}^2} - (K_{(14)(32)} + 2K_{13}) \frac{\mathbf{k}_{12} \cdot \mathbf{k}_{34} \mathbf{k}_{14} \cdot \mathbf{k}_{23}}{K_{12}K_{14}K_{23}K_{34}} \right. \\ & \left. - 2(K_{14} + K_{(34)(21)} + K_{23}) \frac{\mathbf{k}_{12} \cdot \mathbf{k}_{24} \mathbf{k}_{13} \cdot \mathbf{k}_{34}}{K_{12}K_{13}K_{24}K_{34}} \right]. \quad (\text{A16}) \end{aligned}$$

Appendix B: N³LO symmetric nuclear-matter matrix elements

We now turn to the 3N and 4N matrix elements defined as

$$\langle V_{AN} \rangle = \frac{1}{A!} \sum_{\tau_1, \dots, \tau_A} \sum_{\sigma_1, \dots, \sigma_A} \langle 1 \cdots A | \mathcal{A}_A \sum_{i_1 \neq \dots \neq i_A} V_{AN}(i_1, \dots, i_A) | 1 \cdots A \rangle, \quad (\text{B1})$$

entering the symmetric nuclear-matter Hartree-Fock calculation of the N³LO many-body forces.

1. Two-pion-exchange 3N

$$\begin{aligned} \langle V_{3N}^{2\pi} \rangle = & 6 \frac{g_A^2}{f_\pi^2} \left(-2 \frac{\delta c_1 m_\pi^2}{f_\pi^2} \left[\frac{\mathbf{k}_{12} \cdot \mathbf{k}_{23}}{K_{12} K_{23}} + 2 \frac{k_{12}^2}{K_{12}^2} \right] + \frac{\delta c_3}{f_\pi^2} \left[\frac{(\mathbf{k}_{12} \cdot \mathbf{k}_{23})^2}{K_{12} K_{23}} - 2 \frac{k_{12}^4}{K_{12}^2} \right] - \frac{\delta c_4}{f_\pi^2} \frac{(\mathbf{k}_{12} \times \mathbf{k}_{23})^2}{K_{12} K_{23}} \right) \\ & + 6 \left[2 \mathbf{k}_{13}^2 F_{2\pi,1}^{(4)}(-\mathbf{k}_{13}, \mathbf{k}_{13}) - \mathbf{k}_{12} \cdot \mathbf{k}_{13} F_{2\pi,1}^{(4)}(-\mathbf{k}_{12}, \mathbf{k}_{13}) \right] - (\mathbf{k}_{12} \times \mathbf{k}_{13})^2 F_{2\pi,2}^{(4)}(-\mathbf{k}_{12}, \mathbf{k}_{13}), \end{aligned} \quad (\text{B2})$$

with shifts in the low-energy couplings δc_1 , $\delta c_3 = -\delta c_4$, the function $F_{2\pi,1}^{(4)}$ is as given in Appendix A, and

$$F_{2\pi,2}^{(4)}(\mathbf{q}_1, \mathbf{q}_2) = -\frac{9g_A^4}{8\pi f_\pi^6 (q_1^2 + m_\pi^2)(q_2^2 + m_\pi^2)} \left[m_\pi + (4m_\pi^2 + q_1^2 + q_2^2 + 2\mathbf{q}_1 \cdot \mathbf{q}_2) A(|\mathbf{q}_1 + \mathbf{q}_2|) \right]. \quad (\text{B3})$$

2. Two-pion-one-pion-exchange 3N

$$\begin{aligned} \langle V_{3N}^{2\pi 1\pi} \rangle = & 24 \left[F_1(k_{12}) \frac{(\mathbf{k}_{12} \cdot \mathbf{k}_{13})^2}{K_{13}} - F_2(k_{12}) \frac{\mathbf{k}_{12} \cdot \mathbf{k}_{13}}{K_{13}} + F_3(k_{12}) \frac{k_{13}^2}{K_{13}} + F_4(k_{12}) \frac{(\mathbf{k}_{12} \cdot \mathbf{k}_{13})^2}{K_{13}} \right. \\ & \left. + F_5(k_{12}) \frac{k_{13}^2}{K_{13}} - F_6(k_{12}) \frac{\mathbf{k}_{12} \cdot \mathbf{k}_{13}}{K_{13}} - 2F_7(0) \frac{k_{23}^2}{K_{23}} + F_7(k_{12}) \frac{k_{13}^2}{K_{13}} + 4F_8(k_{12}) \frac{\mathbf{k}_{12} \cdot \mathbf{k}_{13}}{K_{13}} \right], \end{aligned} \quad (\text{B4})$$

with structure functions $F_1(q)$ to $F_8(q)$ defined in Eqs. (2.17)–(2.20) of Ref. [30].

3. Pion-ring 3N

$$\begin{aligned} \langle V_{3N}^{\text{ring}} \rangle = & 8 \left[9R_1(-\mathbf{k}_{12}, \mathbf{k}_{13}) + 3k_{12}^2 R_2(-\mathbf{k}_{12}, \mathbf{k}_{13}) - 3\mathbf{k}_{12} \cdot \mathbf{k}_{13} R_3(-\mathbf{k}_{12}, \mathbf{k}_{13}) - 3\mathbf{k}_{12} \cdot \mathbf{k}_{13} R_4(-\mathbf{k}_{12}, \mathbf{k}_{13}) \right. \\ & + 3k_{13}^2 R_5(-\mathbf{k}_{12}, \mathbf{k}_{13}) - 6R_6(-\mathbf{k}_{13}, \mathbf{k}_{13}) + 3R_6(-\mathbf{k}_{12}, \mathbf{k}_{13}) - 2k_{13}^2 R_7(-\mathbf{k}_{13}, \mathbf{k}_{13}) + k_{12}^2 R_7(-\mathbf{k}_{12}, \mathbf{k}_{13}) \\ & + 2k_{13}^2 R_8(-\mathbf{k}_{13}, \mathbf{k}_{13}) - \mathbf{k}_{12} \cdot \mathbf{k}_{13} R_8(-\mathbf{k}_{12}, \mathbf{k}_{13}) + 2k_{13}^2 R_9(-\mathbf{k}_{13}, \mathbf{k}_{13}) - \mathbf{k}_{12} \cdot \mathbf{k}_{13} R_9(-\mathbf{k}_{12}, \mathbf{k}_{13}) \\ & - 6R_{10}(-\mathbf{k}_{13}, \mathbf{k}_{13}) + 3R_{10}(-\mathbf{k}_{12}, \mathbf{k}_{13}) - 6S_1(-\mathbf{k}_{12}, 0) + 3S_1(-\mathbf{k}_{12}, \mathbf{k}_{13}) + 3k_{12}^2 S_2(-\mathbf{k}_{12}, \mathbf{k}_{13}) \\ & \left. - 3\mathbf{k}_{12} \cdot \mathbf{k}_{13} S_3(-\mathbf{k}_{12}, \mathbf{k}_{13}) - 3\mathbf{k}_{12} \cdot \mathbf{k}_{13} S_4(-\mathbf{k}_{12}, \mathbf{k}_{13}) + 3k_{13}^2 S_5(-\mathbf{k}_{12}, \mathbf{k}_{13}) + 9S_6(-\mathbf{k}_{12}, \mathbf{k}_{13}) \right], \end{aligned} \quad (\text{B5})$$

with structure functions R_i and S_i defined in Eqs. (A2) and (A7) of Ref. [30].

4. Two-pion-exchange-contact 3N

$$\langle V_{3N}^{2\pi\text{-cont}} \rangle = \frac{3g_A^2}{\pi f_\pi^4} C_T \left(g_A^2 \left[3m_\pi - \frac{m_\pi^3}{3m_\pi^2 + K_{12}} + (4m_\pi^2 - 3k_{12}^2) A(k_{12}) \right] - \left[m_\pi + (2m_\pi^2 + k_{12}^2) A(k_{12}) \right] \right). \quad (\text{B6})$$

5. Relativistic-corrections 3N

$$\begin{aligned}
\langle V_{3N}^{1/m} \rangle = & 12 \left[2k_{13}^2 F_{1/m}^1(-\mathbf{k}_{13}, \mathbf{k}_{13}) - \mathbf{k}_{12} \cdot \mathbf{k}_{13} F_{1/m}^1(-\mathbf{k}_{12}, \mathbf{k}_{13}) - (\mathbf{k}_{12} \times \mathbf{k}_{13})^2 F_{1/m}^2(-\mathbf{k}_{12}, \mathbf{k}_{13}, \mathbf{P}_{12}, \mathbf{P}_{23}) \right. \\
& - (\mathbf{k}_{12} \times \mathbf{k}_{13}) \cdot (\mathbf{k}_{12} \times \mathbf{P}_{23}) F_{1/m}^3(-\mathbf{k}_{12}, \mathbf{k}_{13}) - (\mathbf{k}_{12} \times \mathbf{P}_{13}) \cdot (\mathbf{k}_{12} \times \mathbf{k}_{13}) F_{1/m}^4(-\mathbf{k}_{12}, \mathbf{k}_{13}) \\
& - \mathbf{k}_{12} \cdot \mathbf{k}_{13} F_{1/m}^5(-\mathbf{k}_{12}, \mathbf{k}_{13}, \mathbf{P}_{12}, \mathbf{P}_{23}, \mathbf{P}_{13}) + (\mathbf{k}_{12} \times \mathbf{k}_{13})^2 F_{1/m}^6(-\mathbf{k}_{12}, \mathbf{k}_{13}) - \mathbf{k}_{12} \cdot \mathbf{P}_{13} F_{1/m}^7(-\mathbf{k}_{12}, \mathbf{k}_{13}) \\
& + k_{12}^2 F_{1/m}^8(-\mathbf{k}_{12}, \mathbf{k}_{13}) + k_{12}^2 F_{1/m}^9(-\mathbf{k}_{12}, \mathbf{k}_{13}) + k_{12}^2 F_{1/m}^{10}(-\mathbf{k}_{12}, \mathbf{P}_{12}, \mathbf{P}_{23}) - \mathbf{k}_{12} \cdot \mathbf{k}_{13} F_{1/m}^{11}(k_{12}) \\
& \left. - \mathbf{k}_{12} \cdot \mathbf{k}_{13} F_{1/m}^{12}(k_{12}) - \mathbf{k}_{12} \cdot \mathbf{P}_{23} F_{1/m}^{13}(k_{12}) - \mathbf{k}_{12} \cdot \mathbf{P}_{12} F_{1/m}^{14}(k_{12}) \right], \tag{B7}
\end{aligned}$$

with

$$F_{1/m}^1(\mathbf{q}_1, \mathbf{q}_2) = -\frac{g_A^4}{16mf_\pi^4} \frac{1}{(q_1^2 + m_\pi^2)(q_2^2 + m_\pi^2)} \left[\frac{1}{(q_1^2 + m_\pi^2)} (1 - 2\bar{\beta}_8)(\mathbf{q}_1 \cdot \mathbf{q}_2)^2 + (2\bar{\beta}_9 - 1)q_1^2 \right], \tag{B8}$$

$$F_{1/m}^2(\mathbf{q}_1, \mathbf{q}_2, \mathbf{q}_3, \mathbf{q}_4) = \frac{g_A^2}{8mf_\pi^4} \frac{1}{(q_1^2 + m_\pi^2)(q_2^2 + m_\pi^2)} \left(\frac{g_A^2}{(q_1^2 + m_\pi^2)} \left[(1 - 2\bar{\beta}_8)\mathbf{q}_1 \cdot \mathbf{q}_4 + (1 + 2\bar{\beta}_8)\mathbf{q}_1 \cdot \mathbf{q}_3 \right] \right), \tag{B9}$$

$$F_{1/m}^3(\mathbf{q}_1, \mathbf{q}_2) = -\frac{g_A^4}{8mf_\pi^4} \frac{2\bar{\beta}_9 - 1}{(q_1^2 + m_\pi^2)(q_2^2 + m_\pi^2)} = -F_{1/m}^4(\mathbf{q}_1, \mathbf{q}_2) \frac{2\bar{\beta}_9 - 1}{2\bar{\beta}_9 + 1}, \tag{B10}$$

$$\begin{aligned}
F_{1/m}^5(\mathbf{q}_1, \mathbf{q}_2, \mathbf{q}_3, \mathbf{q}_4, \mathbf{q}_5) = & \frac{g_A^2}{4mf_\pi^4} \frac{1}{(q_1^2 + m_\pi^2)(q_2^2 + m_\pi^2)} \left(-\frac{g_A^2}{(q_1^2 + m_\pi^2)} \mathbf{q}_1 \cdot \mathbf{q}_2 \left[(1 - 2\bar{\beta}_8)\mathbf{q}_1 \cdot \mathbf{q}_4 + (1 + 2\bar{\beta}_8)\mathbf{q}_1 \cdot \mathbf{q}_3 \right] \right. \\
& \left. + \mathbf{q}_2 \cdot (\mathbf{q}_5 - \mathbf{q}_4) + g_A^2(2\bar{\beta}_9 - 1)\mathbf{q}_1 \cdot \mathbf{q}_4 \right), \tag{B11}
\end{aligned}$$

$$F_{1/m}^6(\mathbf{q}_1, \mathbf{q}_2) = -\frac{g_A^2}{8mf_\pi^4} \frac{1}{(q_1^2 + m_\pi^2)(q_2^2 + m_\pi^2)} \left[\frac{g_A^2}{q_1^2 + m_\pi^2} (1 - 2\bar{\beta}_8) \mathbf{q}_1 \cdot \mathbf{q}_2 + 1 \right], \tag{B12}$$

$$F_{1/m}^7(\mathbf{q}_1, \mathbf{q}_2) = -\frac{g_A^4}{4mf_\pi^4} \frac{(2\bar{\beta}_9 + 1) \mathbf{q}_1 \cdot \mathbf{q}_2}{(q_1^2 + m_\pi^2)(q_2^2 + m_\pi^2)}, \tag{B13}$$

$$F_{1/m}^8(\mathbf{q}_1, \mathbf{q}_2) = \frac{g_A^2}{4mf_\pi^2} C_S \frac{(1 - 2\bar{\beta}_8) \mathbf{q}_1 \cdot \mathbf{q}_2}{(q_1^2 + m_\pi^2)^2} = F_{1/m}^9(\mathbf{q}_1, \mathbf{q}_2) \frac{C_S}{C_T}, \tag{B14}$$

$$F_{1/m}^{10}(\mathbf{q}_1, \mathbf{q}_2, \mathbf{q}_3) = \frac{g_A^2}{mf_\pi^2} \frac{1}{(q_1^2 + m_\pi^2)^2} C_T \left[(1 - 2\bar{\beta}_8) \mathbf{q}_1 \cdot \mathbf{q}_3 + (1 + 2\bar{\beta}_8) \mathbf{q}_1 \cdot \mathbf{q}_2 \right], \tag{B15}$$

$$F_{1/m}^{11}(q) = \frac{g_A^2}{4mf_\pi^2} \frac{2\bar{\beta}_9 - 1}{q^2 + m_\pi^2} C_S = F_{1/m}^{12}(q) \frac{C_S}{C_T} = F_{1/m}^{13}(q) \frac{C_S}{4C_T} = -F_{1/m}^{14}(q) \frac{C_S(2\bar{\beta}_9 - 1)}{4C_T(2\bar{\beta}_9 + 1)}. \tag{B16}$$

6. Three-pion-exchange and pion-interaction 4N

$$\begin{aligned}
\langle V_{4N}^a \rangle = & -\frac{3g_A^6}{4f_\pi^6} \left(4 \left[\frac{k_{14}^2 (\mathbf{k}_{14} \cdot \mathbf{k}_{(14)(23)})^2}{K_{14}^2 K_{(14)(23)}^2} + \frac{\mathbf{k}_{12} \cdot \mathbf{k}_{34} \mathbf{k}_{12} \cdot \mathbf{k}_{14} \mathbf{k}_{34} \cdot \mathbf{k}_{14}}{K_{12} K_{14}^2 K_{34}} - \frac{\mathbf{k}_{12} \cdot \mathbf{k}_{14} \mathbf{k}_{12} \cdot \mathbf{k}_{13} \mathbf{k}_{14} \cdot \mathbf{k}_{13}}{K_{12} K_{13}^2 K_{14}} \right] \right. \\
& + 2 \left[\frac{(\mathbf{k}_{14} \times \mathbf{k}_{42}) \cdot (\mathbf{k}_{31} \times \mathbf{k}_{42}) \mathbf{k}_{14} \cdot \mathbf{k}_{(14)(23)}}{K_{14} K_{(14)(23)}^2 K_{24}} - \frac{(\mathbf{k}_{12} \times \mathbf{k}_{43}) \cdot (\mathbf{k}_{31} \times \mathbf{k}_{43}) \mathbf{k}_{12} \cdot \mathbf{k}_{14}}{K_{12} K_{14}^2 K_{34}} \right. \\
& \quad \left. + \frac{(\mathbf{k}_{12} \times \mathbf{k}_{41}) \cdot (\mathbf{k}_{34} \times \mathbf{k}_{41}) \mathbf{k}_{12} \cdot \mathbf{k}_{13}}{K_{12} K_{13}^2 K_{14}} \right] \\
& - 2 \left[\frac{(\mathbf{k}_{14} \times \mathbf{k}_{42}) \cdot (\mathbf{k}_{14} \times \mathbf{k}_{23}) \mathbf{k}_{42} \cdot \mathbf{k}_{(14)(23)}}{K_{14} K_{(14)(23)}^2 K_{24}} - \frac{(\mathbf{k}_{12} \times \mathbf{k}_{43}) \cdot (\mathbf{k}_{12} \times \mathbf{k}_{24}) \mathbf{k}_{43} \cdot \mathbf{k}_{14}}{K_{12} K_{14}^2 K_{34}} \right. \\
& \quad \left. + \frac{(\mathbf{k}_{12} \times \mathbf{k}_{41}) \cdot (\mathbf{k}_{12} \times \mathbf{k}_{23}) \mathbf{k}_{41} \cdot \mathbf{k}_{13}}{K_{12} K_{13}^2 K_{14}} \right] \\
& + \left[(\mathbf{k}_1 \times \mathbf{k}_2) \cdot \mathbf{k}_{34} + (\mathbf{k}_3 \times \mathbf{k}_4) \cdot \mathbf{k}_{12} \right]^2 \left[\frac{1}{K_{14} K_{(14)(23)}^2 K_{24}} + \frac{1}{K_{12} K_{14}^2 K_{34}} - \frac{1}{K_{12} K_{13}^2 K_{14}} \right] \\
& + 2 \frac{k_{14}^2 (\mathbf{k}_{14} \times \mathbf{k}_{(14)(23)})^2}{K_{14}^2 K_{(14)(23)}^2} - \frac{\mathbf{k}_{14} \cdot \mathbf{k}_{24} (\mathbf{k}_{(14)(23)} \times \mathbf{k}_{14}) \cdot (\mathbf{k}_{(14)(23)} \times \mathbf{k}_{24})}{K_{14} K_{(14)(23)}^2 K_{24}} \\
& \left. + \frac{\mathbf{k}_{12} \cdot \mathbf{k}_{34} (\mathbf{k}_{14} \times \mathbf{k}_{12}) \cdot (\mathbf{k}_{14} \times \mathbf{k}_{34})}{K_{12} K_{14}^2 K_{34}} - \frac{\mathbf{k}_{12} \cdot \mathbf{k}_{14} (\mathbf{k}_{13} \times \mathbf{k}_{12}) \cdot (\mathbf{k}_{13} \times \mathbf{k}_{14})}{K_{12} K_{13}^2 K_{14}} \right), \tag{B17}
\end{aligned}$$

$$\begin{aligned}
\langle V_{4N}^c \rangle = & \frac{3g_A^4}{2f_\pi^6} \left(2 \left[\frac{k_{14}^2 \mathbf{k}_{14} \cdot \mathbf{k}_{(14)(23)}}{K_{14}^2 K_{(14)(23)}} + \frac{\mathbf{k}_{12} \cdot \mathbf{k}_{34} \mathbf{k}_{34} \cdot \mathbf{k}_{14}}{K_{12} K_{14} K_{34}} - \frac{\mathbf{k}_{12} \cdot \mathbf{k}_{14} \mathbf{k}_{14} \cdot \mathbf{k}_{13}}{K_{12} K_{13} K_{14}} \right] \right. \\
& \left. + \left[\frac{(\mathbf{k}_{14} \times \mathbf{k}_{42}) \cdot (\mathbf{k}_{31} \times \mathbf{k}_{42})}{K_{14} K_{(14)(23)} K_{24}} - \frac{(\mathbf{k}_{12} \times \mathbf{k}_{43}) \cdot (\mathbf{k}_{31} \times \mathbf{k}_{43})}{K_{12} K_{14} K_{34}} + \frac{(\mathbf{k}_{12} \times \mathbf{k}_{41}) \cdot (\mathbf{k}_{34} \times \mathbf{k}_{41})}{K_{12} K_{13} K_{14}} \right] \right), \tag{B18}
\end{aligned}$$

$$\begin{aligned}
\langle V_{4N}^e \rangle = & \frac{3g_A^4}{8f_\pi^6} \left[-4 \frac{k_{24}^2}{K_{13} K_{24}^2} \mathbf{k}_{13} \cdot (\mathbf{k}_{13} + \mathbf{k}_{24}) + \frac{\mathbf{k}_{13} \cdot \mathbf{k}_{24}}{K_{13} K_{23} K_{24}} \mathbf{k}_{23} \cdot (\mathbf{k}_{13} + \mathbf{k}_{24}) + 6 \frac{\mathbf{k}_{13} \cdot \mathbf{k}_{34}}{K_{13} K_{24} K_{34}} \mathbf{k}_{24} \cdot \mathbf{k}_{14} \right. \\
& \left. - 2 \frac{\mathbf{k}_{23} \cdot \mathbf{k}_{24}}{K_{13} K_{23} K_{24}} \mathbf{k}_{13} \cdot (\mathbf{k}_{13} + \mathbf{k}_{24}) + 6 \frac{\mathbf{k}_{23} \cdot \mathbf{k}_{14}}{K_{14} K_{23} K_{34}} \mathbf{k}_{34} \cdot \mathbf{k}_{13} + 6 \frac{\mathbf{k}_{12} \cdot \mathbf{k}_{24}}{K_{12} K_{24} K_{34}} \mathbf{k}_{34} \cdot \mathbf{k}_{23} \right], \tag{B19}
\end{aligned}$$

$$\begin{aligned}
\langle V_{4N}^f \rangle = & \frac{3g_A^4}{16f_\pi^6} \left[(6m_\pi^2 + 4K_{(12)(34)}) \frac{k_{12}^2 k_{34}^2}{K_{12}^2 K_{34}^2} + (K_{(14)(32)} - 6K_{13}) \frac{\mathbf{k}_{12} \cdot \mathbf{k}_{34} \mathbf{k}_{14} \cdot \mathbf{k}_{23}}{K_{12} K_{14} K_{23} K_{34}} \right. \\
& \left. - (6K_{14} - 2K_{(34)(21)} + 6K_{23}) \frac{\mathbf{k}_{12} \cdot \mathbf{k}_{24} \mathbf{k}_{13} \cdot \mathbf{k}_{34}}{K_{12} K_{13} K_{24} K_{34}} \right]. \tag{B20}
\end{aligned}$$

7. Two-pion-exchange-contact 4N

$$\langle V_{4N}^k \rangle = -C_T \frac{12g_A^4}{f_\pi^4} \left[\frac{k_{13}^2 k_{24}^2 - (\mathbf{k}_{13} \cdot \mathbf{k}_{24})^2}{K_{13} K_{(13)(24)}^2} - 2 \frac{(\mathbf{k}_{13} \cdot \mathbf{k}_{(13)(24)})^2}{K_{13} K_{(13)(24)}^2} \right], \tag{B21}$$

$$\langle V_{4N}^l \rangle = -C_T \frac{12g_A^2}{f_\pi^4} \frac{\mathbf{k}_{13} \cdot \mathbf{k}_{(13)(24)}}{K_{13} K_{(13)(24)}}, \tag{B22}$$

$$\langle V_{4N}^n \rangle = -C_T^2 \frac{12g_A^2}{f_\pi^4} \frac{\mathbf{k}_{(13)(24)}^2}{K_{(13)(24)}^2}. \tag{B23}$$

-
- [1] E. Epelbaum, H.-W. Hammer, and U.-G. Meißner, *Rev. Mod. Phys.* **81**, 1773 (2009).
- [2] H.-W. Hammer, A. Nogga, and A. Schwenk, *Rev. Mod. Phys.* **85**, 197 (2013).
- [3] I. Tews, T. Krüger, K. Hebeler, and A. Schwenk, *Phys. Rev. Lett.* **110**, 032504 (2013).
- [4] K. Hebeler and A. Schwenk, *Phys. Rev. C* **82**, 014314 (2010).
- [5] K. Hebeler, J. M. Lattimer, C. J. Pethick, and A. Schwenk, *Phys. Rev. Lett.* **105**, 161102 (2010).
- [6] T. Otsuka, T. Suzuki, J. D. Holt, A. Schwenk, and Y. Akaishi, *Phys. Rev. Lett.* **105**, 032501 (2010).
- [7] J. D. Holt, T. Otsuka, A. Schwenk, and T. Suzuki, *J. Phys. G* **39**, 085111 (2012).
- [8] G. Hagen, M. Hjorth-Jensen, G. R. Jansen, R. Machleidt, and T. Papenbrock, *Phys. Rev. Lett.* **108**, 242501 (2012).
- [9] E. Lunderberg *et al.*, *Phys. Rev. Lett.* **108**, 142503 (2012).
- [10] G. Hagen, M. Hjorth-Jensen, G. R. Jansen, R. Machleidt, and T. Papenbrock, *Phys. Rev. Lett.* **109**, 032502 (2012).
- [11] A. T. Gallant *et al.*, *Phys. Rev. Lett.* **109**, 032506 (2012).
- [12] R. Roth, S. Binder, K. Vobig, A. Calci, J. Langhammer, and P. Navrátil, *Phys. Rev. Lett.* **109**, 052501 (2012).
- [13] M. Petri *et al.*, *Phys. Rev. C* **86**, 044329 (2012).
- [14] J. D. Holt, J. Menéndez and A. Schwenk, *Eur. Phys. J. A* **49**, 39 (2013).
- [15] J. D. Holt, J. Menéndez, and A. Schwenk, *Phys. Rev. Lett.* **110**, 022502 (2013).
- [16] C. Caesar, J. Simonis *et al.*, arXiv:1209.0156.
- [17] H. Hergert, S. K. Bogner, S. Binder, A. Calci, J. Langhammer, R. Roth, and A. Schwenk, *Phys. Rev. C* **87**, 034307 (2013).
- [18] A. Lepailleur *et al.*, *Phys. Rev. Lett.* **110**, 082502 (2013).
- [19] H. Hergert, S. Binder, A. Calci, J. Langhammer, and R. Roth, *Phys. Rev. Lett.* **110**, 242501 (2013).
- [20] A. Cipollone, C. Barbieri, and P. Navrátil, arXiv:1303.4900.
- [21] J. D. Holt, J. Menéndez and A. Schwenk, *J. Phys. G* **40**, 075105 (2013).
- [22] E. Epelbaum, H. Krebs, D. Lee, and U.-G. Meißner, *Eur. Phys. J. A* **40**, 199 (2009).
- [23] N. Kaiser, S. Fritsch, and W. Weise, *Nucl. Phys. A* **697**, 255 (2002).
- [24] W. Weise, *Prog. Part. Nucl. Phys.* **67**, 299 (2012).
- [25] S. K. Bogner, A. Schwenk, R. J. Furnstahl, and A. Nogga, *Nucl. Phys. A* **763**, 59 (2005).
- [26] S. K. Bogner, R. J. Furnstahl, and A. Schwenk, *Prog. Part. Nucl. Phys.* **65**, 94 (2010).
- [27] J. W. Holt, N. Kaiser, and W. Weise, *Phys. Rev. C* **87**, 014338 (2013).
- [28] A. Gezerlis, I. Tews, E. Epelbaum, S. Gandolfi, K. Hebeler, A. Nogga, and A. Schwenk, *Phys. Rev. Lett.* **111**, 032501 (2013).
- [29] S. Ishikawa and M. R. Robilotta, *Phys. Rev. C* **76**, 014006 (2007).
- [30] V. Bernard, E. Epelbaum, H. Krebs, and U.-G. Meißner, *Phys. Rev. C* **77**, 064004 (2008). The structure functions R_6 , R_8 , R_9 and R_{10} in Eq. (A.1) need to be corrected by a symmetry factor $\frac{1}{2}$.
- [31] V. Bernard, E. Epelbaum, H. Krebs, and U.-G. Meißner, *Phys. Rev. C* **84**, 054001 (2011).
- [32] E. Epelbaum, *Phys. Lett. B* **639**, 456 (2006).
- [33] E. Epelbaum, *Eur. Phys. J. A* **34**, 197 (2007).
- [34] K. Hebeler, S. K. Bogner, R. J. Furnstahl, A. Nogga and A. Schwenk, *Phys. Rev. C* **83**, 031301(R) (2011).
- [35] E. Epelbaum, W. Glöckle, and U.-G. Meißner, *Eur. Phys. J. A* **19**, 401 (2004).
- [36] E. Epelbaum, W. Glöckle, and U.-G. Meißner, *Nucl. Phys. A* **747**, 362 (2005).
- [37] D. R. Entem and R. Machleidt, *Phys. Rev. C* **68**, 041001(R) (2003).
- [38] R. Machleidt and D. R. Entem, *Phys. Rept.* **503**, 1 (2011).
- [39] U. van Kolck, *Phys. Rev. C* **49**, 2932 (1994).
- [40] E. Epelbaum, A. Nogga, W. Glöckle, H. Kamada, U.-G. Meißner, and H. Witala, *Phys. Rev. C* **66**, 064001 (2002).
- [41] L. Tolos, B. Friman, and A. Schwenk, *Nucl. Phys. A* **806**, 105 (2008).
- [42] E. Epelbaum, *Prog. Part. Nucl. Phys.* **57**, 654 (2006).
- [43] H. Krebs, A. Gasparyan, and E. Epelbaum, *Phys. Rev. C* **85**, 054006 (2012).
- [44] N. Kaiser, *Eur. Phys. J. A* **48**, 135 (2012).
- [45] A. Schwenk and C. J. Pethick, *Phys. Rev. Lett.* **95**, 160401 (2005).
- [46] L. Coraggio, J. W. Holt, N. Itaco, R. Machleidt, and F. Sammarruca, *Phys. Rev. C* **87**, 014322 (2013).
- [47] S. Fiorilla, N. Kaiser, and W. Weise, *Nucl. Phys. A* **880**, 65 (2012).
- [48] A. Gezerlis and J. Carlson, *Phys. Rev. C* **81**, 025803 (2010).
- [49] A. Akmal, V. R. Pandharipande, and D. G. Ravenhall, *Phys. Rev. C* **58**, 1804 (1998).
- [50] S. Gandolfi, J. Carlson, and S. Reddy, *Phys. Rev. C* **85**, 032801(R) (2012).
- [51] J. M. Lattimer and Y. Lim, *Astrophys. J.* **771**, 51 (2013).
- [52] K. Hebeler, J. M. Lattimer, C. J. Pethick, and A. Schwenk, *Astrophys. J.* **773**, 11 (2013).
- [53] M. Kortelainen, T. Lesinski, J. Moré, W. Nazarewicz, J. Sarich, N. Schunck, M. Stoitsov, and S. Wild, *Phys. Rev. C* **82**, 024313 (2010).
- [54] A. Tamii *et al.*, *Phys. Rev. Lett.* **107**, 062502 (2011).
- [55] J. M. Lattimer and F. D. Swesty, *Nucl. Phys. A* **535**, 331 (1991).
- [56] S. Typel (private communication).
- [57] G. Shen, C. J. Horowitz, and E. O'Connor, *Phys. Rev. C* **83**, 065808 (2011).
- [58] G. Shen, C. J. Horowitz, and S. Teige, *Phys. Rev. C* **83**, 035802 (2011).
- [59] A. W. Steiner, M. Hempel, and T. Fischer, arXiv:1207.2184.
- [60] H. Shen, H. Toki, K. Oyamatsu, and K. Sumiyoshi, *Astrophys. J. Suppl.* **197**, 20 (2011).
- [61] G. Shen (private communication).
- [62] M. Hempel (private communication).
- [63] P. B. Demorest, T. Pennucci, S. Ransom, M. Roberts, and J. Hessels, *Nature* **467**, 1081 (2010).
- [64] M. Hempel, T. Fischer, J. Schaffner-Bielich, and M. Liebendörfer, *Astrophys. J.* **748**, 70 (2012).
- [65] E. O'Connor (private communication); A. Kleiner, B.Sc. thesis, Technische Universität Darmstadt, 2012.
- [66] A. Bauswein and H.-T. Janka, *Phys. Rev. Lett.* **108**, 011101 (2012).

- [67] A. Bauswein, H.-T. Janka, K. Hebeler, and A. Schwenk, Phys. Rev. D **86**, 063001 (2012).
- [68] K. Hebeler, Phys. Rev. C **85**, 021002 (2012).
- [69] K. Hebeler and R. J. Furnstahl, Phys. Rev. C **87**, 031302 (2013).
- [70] A. Ekström *et al.*, Phys. Rev. Lett. **110**, 192502 (2013).
- [71] D. Rozpędzik *et al.*, Acta Phys. Polon. B **37**, 2889 (2006).
- [72] H. McManus and D. O. Riska, Phys. Lett. **92B**, 29 (1980).